Hierarchical crystal plasticity FE model for nickel-based superalloys: Sub-grain microstructures to polycrystalline aggregates

Shahriyar Keshavarz, Somnath Ghosh *

Department of Civil Engineering, Johns Hopkins University, Baltimore, MD 21218, United States

ABSTRACT

A hierarchical crystal plasticity constitutive model, comprising three different scales for polycrystalline microstructures of Ni-based superalloys, is developed in this paper. Three scales, dominant in models of polycrystalline Ni-based superalloys, are: (i) the sub-grain scale of $\gamma - \gamma'$ microstructure, characterized by γ' precipitate size and their spacing; (ii) grain-scale characterized by the size of single crystals; and (iii) the scale of polycrystalline representative volume elements. A homogenized activation energy-based crystal plasticity (AE-CP) FEM model is developed for the grain-scale, accounting for characteristic parameters of the sub-grain scale $\gamma - \gamma'$ morphology. A significant advantage of this AE-CP model is that its high efficiency enables it to be effectively incorporated in polycrystalline crystal plasticity FE simulations, while retaining the accuracy of detailed sub-grain level representative volume element (SG-RVE) models. The SG-RVE models are created for variable morphology, e.g., volume fraction, precipitate shape and channel-widths. The sub-grain crystal plasticity model incorporates a dislocation density-based crystal plasticity model augmented with mechanisms of anti-phase boundary (APB) shearing of precipitates. The sub-grain model is homogenized for developing parametric functions of morphological variables in evolution laws of the AE-CP model. Micro-twinning initiation and evolution models are incorporated in the single crystal AE-CP finite element models for manifesting tension–compression asymmetry. In the next ascending scale, a polycrystalline microstructure of Ni-based superalloys is simulated using an augmented AE-CP FE model with micro-twinning. Statistically equivalent virtual polycrystals of the alloy CMSX-4 are created for simulations with the homogenized model. The results of simulations at each scale are compared with experimental data with good agreement.

© 2014 Elsevier Ltd. All rights reserved.

1. Introduction

Ni-based superalloys are widely used in propulsion components of the aerospace industry such as turbine engine blades, disks, casings and liners. These alloys possess a desirable combination of high temperature strength and toughness, oxidation and creep resistance, and high temperature stability (McLean and Cahn, 1996; Sungui et al., 2011), attributed to a sub-grain scale two-phase $\gamma - \gamma'$ microstructure as shown in Fig.1. The continuous γ-matrix phase has a face centered cubic (*fcc*) lattice structure, and is an alloy of Ni and Cr with a small fraction of other alloying elements. The precipitate phase γ' is a coherent ordered inter-metallic reinforcing phase of $L1_2$ crystal structure of Ni₃Al type, which appears as a distribution of cuboidal precipitates in a solid solution as shown in Fig. 1(b). The shape and size of the γ'-phase depend largely on the cooling rate and internal stress gradients during the casting and heat treatment processes (Epishin et al., 2001; Pollock and Sammy, 2006; Ignat et al. 1993). Slower cooling rates lead to the formation of bimodal populations of large (>500 nm) secondary and small (<50 nm) tertiary γ' precipitates, while higher cooling rates yield predominantly unimodal distribution of secondary γ' precipitates (300–500 nm) (Pollock and Sammy, 2006). The γ' precipitates act as effective obstacles to the motion of dislocations by virtue of their shape and ordered structure. Depending on the temperature range and stress levels, dislocations either bypass or shear precipitates. The volume fraction of γ' precipitates, their mean size and spacing have a major effect on the mechanical properties of these superalloys (Viswanathan et al., 2005; Van Sluytman and Pollock, 2012). Micromechanisms controlling creep in polycrystalline Ni-based superalloys are quite complex (Viswanathan et al., 2005; Kovarik et al., 2009). At intermediate temperatures $650\,^\circ\text{C} \leqslant \theta \leqslant 800\,^\circ\text{C}$ and moderate stress levels $\sim$650 MPa, dominant deformation mechanisms include anti-phase boundary (APB) shearing and micro-twinning. The probability of occurrence of a given mechanism depends on the load, crystal orientation and microstructural

---

* Corresponding author. Tel.: +1 410 516 7833; fax: +1 410 516 7473.
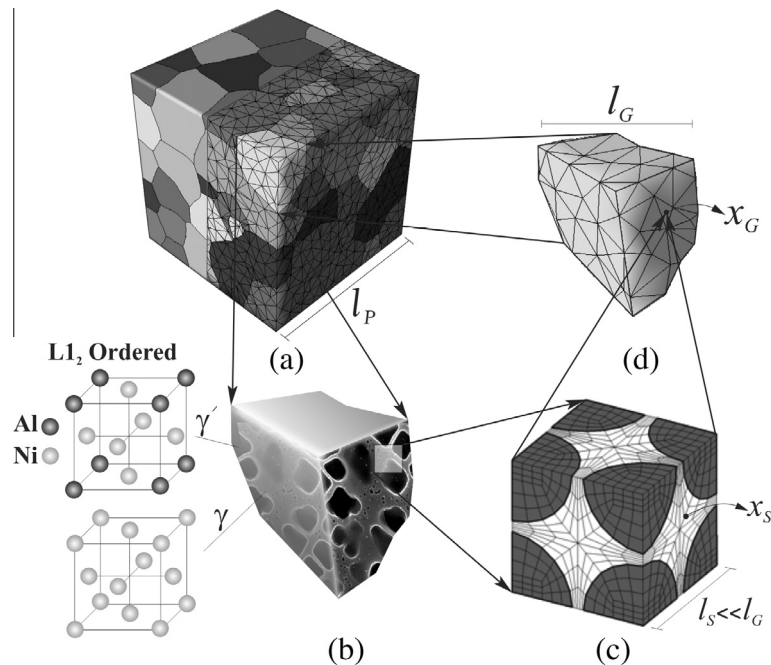 *E-mail address:* sghosh20@jhu.edu (S. Ghosh).

Fig. 1. Schematic representation of multiple scales in the development of a crystal plasticity finite element model for Ni-based superalloys: (a) polycrystalline microstructure showing the CPFEM mesh, (b) subgrain $\gamma - \gamma'$ microstructure in a single grain, (c) discretized subgrain $\gamma - \gamma'$ microstructural RVE, and (d) homogenized crystal plasticity FE model for a grain.

morphology. At lower temperatures ($\theta < 650\,°$C) and higher stresses, creep is governed by different types of dislocation-based shearing processes, while at higher temperatures ($\theta > 800\,°$C), the creep deformation is controlled by Orowan looping and jump mechanisms (Unocic et al., 2011).

Deformation behavior under various loading and temperature conditions has been analyzed both for single crystal (Chatterjee et al., 2010; Cormier et al., 2007) and polycrystalline (Torster et al., 1997; Hong et al., 2009) Ni-based superalloys. Meso-scale modeling of the $\gamma - \gamma'$ phases in single crystal Ni-base superalloys with unimodal precipitate sizes and periodic distributions has been conducted in (Pollock and Argon, 1992; Nouailhas and Cailletaud, 1996; Ohashi et al., 1997; Busso et al., 2000) using phenomenological viscoplastic constitutive laws. Crystal plasticity finite element models (CPFEM) have been implemented to model creep and deformation response of single crystal and polycrystalline Ni-based superalloys in (Dimiduk et al., 2005; Choi et al., 2005; Zambaldi et al., 2007; Roters et al. 2010). In these models, the behavior of single-crystal superalloys with high volume fraction of cuboidal precipitates has been simulated using a gradient-dependent plasticity model. Polycrystalline CPFEM simulations incorporate information on the orientation of grains obtained from EBSD images of the material microstructure. Phenomenological crystal plasticity models are based on the power law description (Asaro and Needleman, 1985), or the thermally activated theory of plastic law (Kocks et al., 1975), which accounts for the rate and temperature sensitivity of plastic flow. The latter model has been shown to accurately model a large range of strain rates and temperatures. A limitation of the above models for Ni-based superalloys is their lack of incorporation of the underlying microstructural characteristics at the sub-grain scale, e.g., $\gamma - \gamma'$ volume fraction, shape of the γ' precipitates and the γ channel-width, which affect the single crystal and polycrystalline behavior.

Three scales are dominant when modeling polycrystalline behavior of Ni-based superalloys using CPFEM. They are:

i. Sub-grain scale, characterized by the size of γ' precipitates and their spacing or γ channel-width;

ii. Grain-scale of single crystals characterized by grain-boundary distance;

iii. Scale corresponding to representative volume elements of polycrystalline aggregates.

Crystal plasticity models should hierarchically incorporate information at each scale for generating constitutive models that can be implemented for microstructure–property relations, as well as microstructure design. It is computationally intractable to simulate the behavior of polycrystalline microstructures with explicit representation of the $\gamma - \gamma'$ microstructure. While analytical models have been proposed to overcome this limitation using simplifying assumptions for dislocation distribution in Probst et al. (1999), they are not appropriate for multi-axial or non-monotonic loading histories. In Busso et al. (2000), hardening parameters are expressed as functions of the average size of precipitates. Crystal plasticity models with implicit dependencies on grain and precipitate sizes and volume fraction, have been proposed in Fedelich (2002) by assuming random distribution of precipitate phases. Computational models involving hierarchical approaches for Ni-based superalloys have been proposed in Shenoy et al. (2007), Shenoy (2006), and Song (2010). In Shenoy et al. (2007) and Shenoy (2006), dislocation-density based crystal plasticity models for creep and fatigue have been developed using artificial neural network algorithm for rate-dependent internal state variable constitutive models, implicitly incorporating effects of averaged grain size, γ' volume fraction and size distribution. The dependence of strength and hardness on microstructural parameters is accommodated by fitting with experimental data. The models of Shenoy (2006) have been extended in Song (2010) for different temperature ranges and load histories. The stress for nucleating dislocations has been expressed as a functional form of the volume fraction and the size of precipitates in Fromm et al. (2012).

It is evident that efficient, hierarchical crystal plasticity models with explicit relations to microstructural features are necessary for unraveling the dependence of mechanical behavior and properties on microstructure. The hierarchical framework may be accomplished for Ni-based superalloys through the homogenization of

lower (sub-grain) scale response to develop higher (grain) scale constitutive relations. This is achieved by incorporating parametric forms of subgrain-scale morphological characteristics in grain-level constitutive relations. Ghosh et. al. have implemented computational homogenization approaches using asymptotic expansion methods to develop reduced order homogenized constitutive models for continuum plasticity of polycrystalline metals (Ghosh and Anahid, 2013), ductile fracture in heterogeneous metals (Ghosh et al., 2009; Ghosh, 2011) and damage in composites (Jain and Ghosh, 2008). These reduced order models with parametric forms, representing microstructural morphologies, have a huge efficiency advantage over explicit micromechanics models. In a recent paper (Keshavarz and Ghosh, 2013), the authors have developed a hierarchical model for Ni-based superalloys, where the sub-grain-scale model response is homogenized to obtain a grain-scale crystal plasticity constitutive model. The present work extends this work to include polycrystalline microstructure modeling in a three-scale hierarchical modeling framework.

In this paper a sequence of steps is pursued to systematically create a hierarchical framework for realizing a homogenized crystal plasticity constitutive model for polycrystalline Ni-based superalloys. The crystal plasticity models account for monotonic loading only and cyclic loading is not considered in this paper. A schematic view of the multi-scale problem, ranging from the sub-grain $\gamma - \gamma'$ microstructure to the meso-scale polycrystalline ensemble is shown in Fig. 1. The first step involves development of crystal plasticity finite element (CPFE) model of a sub-grain scale representative volume element or RVE, delineating explicit morphologies of the $\gamma - \gamma'$ microstructure shown in Fig. 1(c). The CPFE model incorporates a size-dependent dislocation density-based crystal plasticity model together with the mechanism considered in this study of anti-phase boundary (APB) shearing of γ' precipitates. Experimental studies have shown that mechanisms such as APB and microtwinning are important at the temperature range ($650\,^{\circ}$C $\leqslant \theta \leqslant 800\,^{\circ}$C). In this temperature range, dislocation glide on the primary octahedral plane (1 1 1) are responsible for plastic deformation and hence cube slip systems on (0 0 1) plane are ignored in this study. Section 2 introduces the sub-grain scale dislocation density crystal plasticity constitutive laws with APB shearing of γ' precipitates. The next step involves the development of an activation energy-based crystal plasticity (AE-CP) model at the scale of single crystals, by homogenizing the sub-grain model response. The homogenized model incorporates the sub-grain morphology through critical morphological parameters (Keshavarz and Ghosh, 2013). Section 3 provides a framework for the AE-CP model and homogenization. This section also introduces nucleation and evolution models for micro-twins in the grain. The final step involves augmentation of the homogenized AE-CP model, accounting for the effects of geometrically necessary dislocations or GND's, for analyzing polycrystalline microstructures. This is developed in Section 4.

The authors recognize that the limits of the continuum theory of dislocation density evolution may be reached for the nano-channels with the dislocation density-based crystal plasticity model used in this study. Explicit representation of dislocation networks is not realized in this formulation. Alternate methods like 3D phase field or discrete dislocation dynamics (DDD) models e.g., (Haghighat et al. 2013) are making advances in understanding different deformation and creep processes. However these models are still evolving and are not yet able to completely represent necessary mechanics and multi-phase morphology necessary for this study. Additionally, the interfaces between these methods and continuum models are still not well defined, especially in 3D. In view of this discussion, the dislocation density based model is considered the most viable option at this time.

2. Sub-grain scale model for the $\gamma - \gamma'$ microstructural RVE

The two-phase binary Ni-based superalloy consists of a primary matrix γ phase (pure Ni) and a secondary intermetallic γ'(Ni$_3$Al) phase as shown in Fig. 1(b). The primary phase is a solid solution with a face-centered cubic or fcc crystal structure, with four planes of inelastic slip corresponding to the {1 1 1} family, i.e., γ in Miller indices. The secondary γ' phase has an ordered crystalline lattice of type $L1_2$. Atoms of aluminum are placed at the vertices of the cubic cell, while atoms of Ni are located at centers of the faces as shown in Fig. 1(b). For each of slip plane, there are three slip directions of $\langle 110 \rangle$ family along the Burgers vectors. Dislocations dissociate in the γ'-phase, leading to formation of an anti-phase boundary (APB). Slip system details in the reference configuration are given in Table 1.

Ni-based superalloys exhibit anisotropic behavior in the plastic regime due to slip system interactions in the $\gamma - \gamma'$ sub-grain microstructure. Plastic deformation is accommodated through crystallographic slip on discrete slip systems and by APB shearing of the γ' phase. A signed dislocation density-based crystal plasticity model proposed in Ma and Roters (2004) and Ma et al. (2006) is implemented in this paper to model rate-dependent plastic behavior. These models incorporate evolution of statistically stored (SSD) and geometrically necessary dislocations (GND) due to the plastic deformation. Plastic strain gradient at the $\gamma - \gamma'$ phase interface and grain boundaries lead to generation of GNDs. The micromechanical crystal plasticity model accommodates multiplication and annihilation of SSDs in the γ-channel and also accounts for APB shearing of γ' precipitates by matrix dislocations.

2.1. Dislocation density-based crystal plasticity model

Crystal deformation results from a combination of the elastic stretching and rotation of the crystal lattice and plastic slip on different slip systems. Large-strain kinematics is accommodated through a multiplicative decomposition of the total deformation gradient $\boldsymbol{F}$ into an incompressible, inelastic component $\boldsymbol{F}^p$ associated with pure slip, and an elastic component $\boldsymbol{F}^e$ that accounts for elastic stretching and rigid-body rotations (Asaro and Rice, 1977), expressed as:

$$\boldsymbol{F} = \boldsymbol{F}^e \boldsymbol{F}^p, \ s.t. \ det\,\boldsymbol{F}^e > 1 \quad \text{and} \quad det\,\boldsymbol{F}^p = 1 \tag{1}$$

Evolution of plastic deformation is expressed in terms of the plastic velocity gradient $\boldsymbol{L}^p$, the plastic shear rate $\dot{\gamma}^\alpha$ on the slip system α, Schmid tensor $\boldsymbol{s}_0^\alpha \equiv \boldsymbol{m}_0^\alpha \otimes \boldsymbol{n}_0^\alpha$ (in terms of the slip direction $\boldsymbol{m}_0^\alpha$ and slip plane normal $\boldsymbol{n}_0^\alpha$ in the reference configuration) as:

$$\boldsymbol{L}^p = \dot{\boldsymbol{F}}^p \boldsymbol{F}^{-p} = \sum_{\alpha=1}^{N} \dot{\gamma}^\alpha \boldsymbol{m}_0^\alpha \otimes \boldsymbol{n}_0^\alpha = \sum_{\alpha=1}^{N} \dot{\gamma}^\alpha \boldsymbol{s}_0^\alpha \tag{2}$$

The stress–strain relation invokes the second Piola–Kirchhoff stress $\boldsymbol{S}$ and its work-conjugate Lagrange–Green strain tensor $\boldsymbol{E}^e$ in the intermediate configuration as:

$$\boldsymbol{S} = det(\boldsymbol{F}^e)\boldsymbol{F}^{e-1}\boldsymbol{\sigma}\boldsymbol{F}^{e-T} = \boldsymbol{C} : \boldsymbol{E}^e \quad \text{and} \quad \boldsymbol{E}^e \equiv \frac{1}{2}\{\boldsymbol{F}^{eT}\boldsymbol{F}^e - \boldsymbol{l}\} \tag{3}$$

$\boldsymbol{I}$ is the identity tensor, $\boldsymbol{C}$ is a fourth order anisotropic elasticity tensor and σ is the Cauchy stress tensor. The plastic shearing rate on a slip system α is expressed using the Orowan equation as $\dot{\gamma}^\alpha = \rho_m^\alpha b v^\alpha$, where ρ_m^α is the density of mobile dislocations, b is the Burgers vector and v^α is the velocity of dislocations on the slip system α. The velocity of dislocations, which is a function of the applied shear stress τ^α, the passing stress τ_{pass}^α in the slip system and other slip system resistances, is written as:

Table 1
Slip systems for fcc materials.

Slip system no.	Slip direction $\mathbf{m_0^\alpha}$	Normal to slip plane $\mathbf{n_0^\alpha}$	Tangent vector $\mathbf{t_0^\alpha}$
1	$\frac{1}{\sqrt{2}}[0\ \bar{1}\ 1]$	$\frac{1}{\sqrt{3}}[1\ 1\ 1]$	$\frac{1}{\sqrt{6}}[2\ \bar{1}\ \bar{1}]$
2	$\frac{1}{\sqrt{2}}[\bar{1}\ 1\ 0]$	$\frac{1}{\sqrt{3}}[1\ 1\ 1]$	$\frac{1}{\sqrt{6}}[\bar{1}\ \bar{1}\ 2]$
3	$\frac{1}{\sqrt{2}}[1\ 0\ \bar{1}]$	$\frac{1}{\sqrt{3}}[1\ 1\ 1]$	$\frac{1}{\sqrt{6}}[\bar{1}\ 2\ \bar{1}]$
4	$\frac{1}{\sqrt{2}}[1\ 0\ 1]$	$\frac{1}{\sqrt{3}}[1\ \bar{1}\ \bar{1}]$	$\frac{1}{\sqrt{6}}[\bar{1}\ \bar{2}\ 1]$
5	$\frac{1}{\sqrt{2}}[0\ 1\ \bar{1}]$	$\frac{1}{\sqrt{3}}[1\ \bar{1}\ \bar{1}]$	$\frac{1}{\sqrt{6}}[2\ 1\ 1]$
6	$\frac{1}{\sqrt{2}}[\bar{1}\ \bar{1}\ 0]$	$\frac{1}{\sqrt{3}}[1\ \bar{1}\ \bar{1}]$	$\frac{1}{\sqrt{6}}[\bar{1}\ 1\ \bar{2}]$
7	$\frac{1}{\sqrt{2}}[\bar{1}\ 0\ \bar{1}]$	$\frac{1}{\sqrt{3}}[\bar{1}\ \bar{1}\ 1]$	$\frac{1}{\sqrt{6}}[1\ \bar{2}\ \bar{1}]$
8	$\frac{1}{\sqrt{2}}[0\ 1\ 1]$	$\frac{1}{\sqrt{3}}[\bar{1}\ \bar{1}\ 1]$	$\frac{1}{\sqrt{6}}[\bar{2}\ 1\ \bar{1}]$
9	$\frac{1}{\sqrt{2}}[1\ \bar{1}\ 0]$	$\frac{1}{\sqrt{3}}[\bar{1}\ \bar{1}\ 1]$	$\frac{1}{\sqrt{6}}[1\ 1\ 2]$
10	$\frac{1}{\sqrt{2}}[\bar{1}\ 0\ 1]$	$\frac{1}{\sqrt{3}}[\bar{1}\ 1\ \bar{1}]$	$\frac{1}{\sqrt{6}}[1\ 2\ 1]$
11	$\frac{1}{\sqrt{2}}[0\ \bar{1}\ \bar{1}]$	$\frac{1}{\sqrt{3}}[\bar{1}\ 1\ \bar{1}]$	$\frac{1}{\sqrt{6}}[\bar{2}\ \bar{1}\ 1]$
12	$\frac{1}{\sqrt{2}}[1\ 1\ 0]$	$\frac{1}{\sqrt{3}}[\bar{1}\ 1\ \bar{1}]$	$\frac{1}{\sqrt{6}}[1\ \bar{1}\ \bar{2}]$

$$v^\alpha = \lambda\upsilon\exp\left\{-\frac{Q_{act}}{k_B\theta}\left(1-\frac{\langle|\tau^\alpha|-\tau^\alpha_{pass}\rangle}{\tau^\alpha_{cut}}\right)\right\}\text{sgn}(\tau^\alpha) \qquad (4)$$

where λ is the distance traversed by dislocations subject to the probability of overcoming barriers, υ is the oscillation frequency of dislocations, Q_{act} the activation free energy required to overcome the obstacles to slip without the aid of an applied shear stress, k_B is the Boltzmann's constant, $\theta\ ^\circ$K is the absolute temperature and $\langle\bullet\rangle$ is the Macaulay bracket. Slip system resistances are represented in terms of the passing stress τ^α_{pass} due to the interaction of mobile dislocations with other dislocations and their networks in the slip plane, and the cutting stress τ^α_{cut} due to the mobile dislocations cutting the forest dislocations with density ρ^α_F perpendicular to the slip plane. The stresses are expressed in Keshavarz and Ghosh (2013) as:

$$\tau^\alpha_{pass} = c_1 Gb\sqrt{\rho^\alpha_P + \rho^\alpha_m} \quad\text{and}\quad \tau^\alpha_{cut} = \frac{Q\sqrt{\rho^\alpha_F}}{c_2 b^2} \qquad (5)$$

where c_1 and c_2 are material constants and G is the shear modulus and Q is the activation energy.

Contributions to the overall slip resistance are assumed to be due to both the density of immobile, statistically stored dislocations ρ^α_{SSD}, and the vector field of geometrically necessary dislocation density $\boldsymbol{\rho}^\alpha_{GND}$. The rate of evolution of statistically stored dislocation density $\dot{\rho}^\alpha_{SSD}$ has been identified in Ma et al. (2006) as the net effect of components due to lock formation, dipole formation, athermal annihilation and thermal annihilation as:

$$\dot{\rho}^\alpha_{SSD} = \dot{\rho}^{\alpha+}_{SSD_{lf}} + \dot{\rho}^{\alpha+}_{SSD_{df}} + \dot{\rho}^{\alpha-}_{SSD_{aa}} + \dot{\rho}^{\alpha-}_{SSD_{ta}} \qquad (6)$$

Superscripts $+/-$ correspond to multiplication and annihilation respectively. The rate increase due to lock formation, dipole formation, and decrease due to mechanisms of dislocation annihilation due to thermal and athermal annihilation are respectively given as (Ma and Roters, 2004):

$$\dot{\rho}^\alpha_{SSD_{lf}} = \frac{c_3}{b}\sqrt{\rho^\alpha_F}\dot{\gamma}^\alpha \quad\text{and}\quad \dot{\rho}^\alpha_{SSD_{df}} = \frac{c_4}{b}\frac{\sqrt{3}Gb}{16\pi(1-\nu)}(|\tau^\alpha|-\tau^\alpha_{pass})^{-1}\rho^\alpha_m\dot{\gamma}^\alpha$$

$$\dot{\rho}^\alpha_{SSD_{aa}} = -c_5\rho^\alpha_{SSD}\dot{\gamma}^\alpha \quad\text{and}\quad \dot{\rho}^\alpha_{SSD_{ta}} = -c_6\frac{D_0 b^3}{k_B\theta}\exp\left(\frac{-Q_{bulk}}{k_B\theta}\right)(\rho^\alpha_{SSD})^2|\tau^\alpha|\left(\frac{\dot{\gamma}^\alpha}{\dot{\gamma}_{ref}}\right)^{c_7} \qquad (7)$$

where c_3, c_4, c_5, c_6 and c_7 are material constants, D_0 is the diffusion co-efficient, Q_{bulk} is the activation energy for dislocation climb and $\dot{\gamma}_{ref}$ is a reference shear rate. Each of the contributing components in Eq. (7) are functions of the slip rate $\dot{\gamma}^\alpha$, forest dislocation density, density of statistically stored dislocations, component of applied shear stress τ^α and the absolute temperature θ. Thus, a general

form is proposed as $\dot{\rho}^\alpha_{SSD} = \dot{\rho}^\alpha_{SSD}(\dot{\gamma}^\alpha, \rho^\alpha_{SSD}, \rho_F, \tau^\alpha, \theta)$. The vector GND density rates depend on the gradient of plastic strain, written in terms of the Nye's dislocation tensor $\boldsymbol{\Lambda}$ (Nye 1953). The three scalar components, viz. screw, edge and normal components of the GND density have been derived in Ma et al. (2006). The material time derivative of the Nye's dislocation tensor is decomposed for individual slip systems, i.e., $\dot{\boldsymbol{\Lambda}} = (\sum_{\alpha=1}^N \dot{\boldsymbol{\Lambda}}^\alpha)$ to derive the GND density components as:

$$\dot{\rho}^\alpha_{GNDs} = \frac{1}{b}[\nabla_X \times (\dot{\gamma}^\alpha \boldsymbol{F}_P^T \boldsymbol{n}_\alpha)]\cdot\boldsymbol{m}^\alpha,$$

$$\rho^\alpha_{GNDet} = \frac{1}{b}[\nabla_X \times (\dot{\gamma}^\alpha \boldsymbol{F}_P^T \boldsymbol{n}_\alpha)]\cdot\boldsymbol{t}_\alpha,$$

$$\dot{\rho}^\alpha_{GNDen} = \frac{1}{b}[\nabla_X \times (\dot{\gamma}^\alpha \boldsymbol{F}_P^T \boldsymbol{n}_\alpha)]\cdot\boldsymbol{n}_\alpha \qquad (8)$$

where $\boldsymbol{m}^\alpha$, $\boldsymbol{n}_\alpha$ and $\boldsymbol{t}_\alpha = (\boldsymbol{n}_\alpha \times \boldsymbol{m}^\alpha)$ are unit vectors in the slip direction of the Burgers vector, normal to the slip plane α, and tangent to the edge dislocation direction respectively. Correspondingly, $\dot{\rho}^\alpha_{GNDs}$, $\dot{\rho}^\alpha_{GNDet}$ and $\dot{\rho}^\alpha_{GNDen}$ are the screw component and two edge components parallel to $\boldsymbol{n}_\alpha$ and $\boldsymbol{t}_\alpha$, respectively. ∇_X is the gradient operator in the material coordinate system. The forest and parallel dislocation densities are now written as functions of the SSDs and GNDs (Ma and Roters, 2004) with an interaction strength coefficient $\chi^{\alpha\beta}$ between different slip systems (Arsenlis and Parks, 2002), as:

$$\rho^\alpha_F = \sum_{\beta=1}^N \chi^{\alpha\beta}[\rho^\beta_{SSD}|\cos(\boldsymbol{n}_\alpha, \boldsymbol{t}^\beta)| + \rho^\beta_{GNDs}|\cos(\boldsymbol{n}_\alpha, \boldsymbol{m}^\beta)|$$
$$+ \rho^\beta_{GNDet}|\cos(\boldsymbol{n}_\alpha, \boldsymbol{t}^\beta)| + \rho^\beta_{GNDen}|\cos(\boldsymbol{n}_\alpha, \boldsymbol{n}^\beta)|]$$
$$\rho^\alpha_P = \sum_{\beta=1}^N \chi^{\alpha\beta}[\rho^\beta_{SSD}|\sin(\boldsymbol{n}_\alpha, \boldsymbol{t}^\beta)| + \rho^\beta_{GNDs}|\sin(\boldsymbol{n}_\alpha, \boldsymbol{m}^\beta)|$$
$$+ \rho^\beta_{GNDet}|\sin(\boldsymbol{n}_\alpha, \boldsymbol{t}^\beta)| + \rho^\beta_{GNDen}|\sin(\boldsymbol{n}_\alpha, \boldsymbol{n}^\beta)|] \qquad (9)$$

which evolve with the SSDs and GNDs due to plastic deformation and hardening mechanisms. The density of mobile dislocations ρ^α_m is computed as a function of forest and parallel dislocation density and the temperature as (Ma and Roters, 2004):

$$\rho^\alpha_m = \frac{2k_B\theta\sqrt{\rho^\alpha_F\rho^\alpha_P}}{c_1 c_2 Gb^3} \qquad (10)$$

2.2. Criteria for γ' phase anti-phase boundary (APB) shearing

Matrix dislocations in the disordered *fcc* matrix γ phase cannot enter the ordered γ' phase, characterized by crystalline lattice structure $L1_2$, initially. However, the matrix dislocations can form super-dislocations at the $\gamma - \gamma'$ interface and enter the γ' phase through the mechanism of anti-phase boundary or APB shearing upon reaching a critical condition, as shown by TEM analysis in Viswanathan et al. (2005). The γ' phase APB shearing is assumed to take place when the following conditions are met at the interface:

(i) $\tau^\alpha > \tau_c$ (resolved shear stress on a slip system exceeds a critical value)

(ii) $\rho^\alpha_m > \rho_c$ (dislocation density exceeds a critical value)

$$(11)$$

The corresponding flow rule for the γ' phase is expressed as:

$$\dot{\gamma}^\alpha = \mathbf{H}(\rho^\alpha_m - \rho_c)\rho^\alpha_m b\upsilon^\alpha \quad\text{where}$$
$$\upsilon^\alpha = \lambda\upsilon\exp\left\{-\frac{Q}{K_B T}\left(1-\frac{\langle\tau^\alpha - \tau^\alpha_{pass}\rangle\mathbf{H}(\tau^\alpha-\tau_c)}{\tau^\alpha_{cut}}\right)\right\}\text{sgn}(\tau^\alpha) \qquad (12)$$

where $\mathbf{H}(\rho_m^\alpha - \rho_c)$ and $\mathbf{H}(\tau^\alpha - \tau_c)$ are Heaviside functions, τ_c is the critical resolved shear stress and ρ_c is the critical density at the interface.

2.3. Implementation of the constitutive model to the CPFEM code and time-integration

Rate-dependent crystal plasticity equations for the γ and γ' phases are implemented in the CPFEM code, using an implicit time-integration scheme. Implicit schemes (Kalidindi, 1998) using the backward Euler time integration methods, solve a set of nonlinear algebraic equations in each time interval $t \leqslant \tau \leqslant t + \Delta t$ using iterative Newton Raphson or Quasi-Newton solvers. The integration requires known deformation variables e.g., $\mathbf{F}(t)$ and $\mathbf{F}^p(t)$, $\rho_{\mathrm{GNDs}}(t)$ and $\rho_{\mathrm{SSD}}(t)$, and slip system deformation resistances $\tau_{pass}(t)$ and $\tau_{cut}(t)$ at time t, as well as $\mathbf{F}(t + \Delta t)$, as inputs to a material update routine CPFEM-MAT. Integrating Eq. (2), the plastic part of deformation gradient at time $t + \Delta t$ is expressed as:

$$\mathbf{F}^p(t+\Delta t) = \left(\mathbf{I} + \sum_{\alpha=1}^N \Delta \dot{\gamma}^\alpha \mathbf{m}_0^\alpha \otimes \mathbf{n}_0^\alpha\right) \mathbf{F}^p(t) = \left(\mathbf{I} + \sum_{\alpha=1}^N \Delta \dot{\gamma}^\alpha \mathbf{s}_0^\alpha\right) \mathbf{F}^p(t) \quad (13)$$

Substituting the expressions for $F^p(t + \Delta t)$ and $F(t + \Delta t)$ into Eqs. (1) and (3), the incremented second Piola–Kirchhoff stress is calculated as:

$$\mathbf{S}(t+\Delta t) = \frac{1}{2}\mathbf{C} : (\mathbf{F}^{p^{-T}}(t+\Delta t)\mathbf{F}^T(t+\Delta t)\mathbf{F}(t+\Delta t)\mathbf{F}^{p^{-1}}(t+\Delta t) - \mathbf{I})$$

$$= \frac{1}{2}\mathbf{C} : [\mathbf{A}(t+\Delta t) - \mathbf{I}] - \sum_\alpha \Delta\gamma^\alpha (\mathbf{S}(t+\Delta t), \tau_{pass}^\alpha(t+\Delta t),$$

$$\tau_{cut}^\alpha(t+\Delta t))\overline{\mathbf{C}}^\alpha = \mathbf{S}^{tr} - \sum_\alpha \Delta\gamma^\alpha (\mathbf{S}(t+\Delta t), \tau_{pass}^\alpha(t+\Delta t),$$

$$\tau_{cut}^\alpha(t+\Delta t)) \, \overline{\mathbf{C}}^\alpha \quad (14)$$

where

$$\mathbf{A}(t+\Delta t) = \mathbf{F}^{p^{-T}}(t)\mathbf{F}^T(t+\Delta t)\mathbf{F}(t+\Delta t)\mathbf{F}^{p^{-1}}(t) \quad \text{and}$$

$$\overline{\mathbf{C}}^\alpha = \frac{1}{2}\mathbf{C} : [\mathbf{A}\mathbf{s}_0^\alpha + \mathbf{s}_0^{\alpha T}\mathbf{A}] \quad (15)$$

The second Piola–Kirchhoff stress in Eq. (14) is solved by using a nonlinear Newton–Raphson iterative solver:

$$\mathbf{S}^{i+1}(t+\Delta t) = \mathbf{S}^i(t+\Delta t) - \left[\mathbf{I} + \sum_\alpha \mathbf{C}^\alpha \otimes \frac{\partial(\Delta\gamma^\alpha)}{\partial \mathbf{S}^i}\right]^{-1} [\mathbf{G}^i] \quad \text{where}$$

$$\mathbf{G} = \mathbf{S} - \mathbf{S}^{tr} + \sum_\alpha \Delta\gamma^\alpha \mathbf{C}^\alpha \quad (16)$$

Subsequently the plastic deformation gradient, Cauchy stress and the tangent stiffness matrix $W_{ijkl} = \frac{\partial \sigma_{ij}}{\partial \varepsilon_{kl}}$ are computed in CPFEM-MAT and passed on to the FE program for equilibrium calculations. The time integration scheme is detailed in Table 2.

2.4. Parameter calibration and validation of the constitutive law

Selected constitutive parameters in the crystal plasticity model for $\gamma - \gamma'$ phase Ni-based superalloys with APB shearing have been calibrated for the alloy CMSX-4 (Ni, Cr-6.4, Co-9.3, Al-5.45, Ta-6.3, W-6.2, Ti-0.9, Mo-0.5, Re-2.8 in wt%) in Keshavarz and Ghosh (2013). Calibration of constants c_1 and c_2 in Eq. (5) and constants c_3, c_4, c_5, c_6 and c_7 in Eq. (7) are done using experimental data from tensile constant strain-rate tests in Knowles and Gunturi (2002). The critical shear stress τ_c and the threshold dislocation density ρ_c in Eq. (11) are calibrated from the tension creep experimental data in Fleury et al. (1996). These are listed in Table 3.

The symmetric, elastic stiffness tensor $\mathbf{C}_{\alpha\beta} = \mathbf{C}_{\beta\alpha}(\alpha = 1 \ldots 6, \beta = 1 \ldots 6)$ is considered to be isotropic for both phases, for which the non-zero components are obtained from (Kayser and Stassis, 1981). In addition, the Burgers vector b and the activation energy Q are obtained from handbook values, given in Table 4.

To validate the crystal plasticity constitutive relations with APB shearing, the CPFEM analyses results are compared with experimental data in Fleury et al. (1996) and Knowles and Gunturi (2002). The RVE is for a regular array of cubic precipitates with a 70% volume fraction, as shown in Fig. 2(a). Its dimensions are $0.5\,\mu m \times 0.5\,\mu m \times 0.5\,\mu m$. The edge length of cubic γ' particles, allocated symmetrically at the eight corners, is $0.45\,\mu m$. The CPFE model of the microstructural RVE is discretized into 2200, 8-noded brick elements using selective reduced integration. CPFEM simulations are conducted with an applied strain-rate of $0.0001\,s^{-1}$ in the y-direction at a temperature of $800\,°C$. To emulate experimental conditions, a tensile constant strain-rate is applied to the top y-surface in Fig. 2(a), while rigid body modes are suppressed by applying boundary conditions on the bottom y-surface as: $u_y = 0$ on all nodes $u_x = 0$ on nodes on the line $x = 0.25\,\mu m$ and $u_z = 0$ on nodes on the line $z = 0.25\,\mu m$.

The volume-averaged Cauchy stresses $\overline{\boldsymbol{\sigma}} = \frac{1}{\Omega_{RVE}} \int_{\Omega_{RVE}} \boldsymbol{\sigma}(\mathbf{x}, t) \, dV$ over the RVE Ω_{RVE} and the averaged true (logarithmic) strain expressed as: $\overline{\boldsymbol{\varepsilon}} = \ln\left(\frac{l_y}{l_{0y}}\right) = \ln\left(\frac{l_{0y} + \overline{u}_y}{l_{0y}}\right)$ are computed for the RVE where l_{0y} and $\overline{u}_y$ are respectively the initial dimension and the y-direction displacement of the top surface of the RVE. The volume-averaged stress–strain response is compared with experimental data from (Fleury et al. 1996) in Fig. 2(b). In general there is a good agreement between the experimental and model predictions. A small divergence with increasing strain may be attributed to the assumed simple RVE with symmetric distribution and
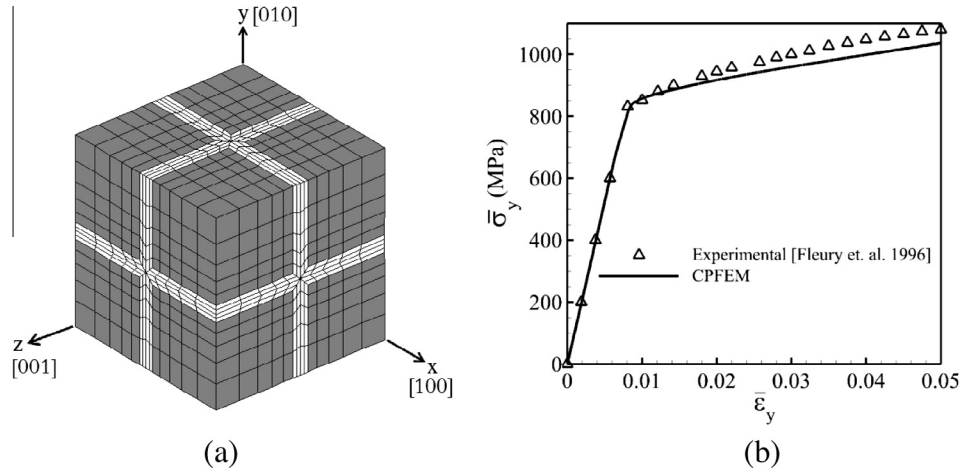
Table 2
Time integration scheme in CPFEM-MAT.

A. For time increment from t to $t + \Delta t$, with known $\mathbf{F}(t + \Delta t)$ and other variables at time t

    i. Calculate $\mathbf{S}^{tr} = \frac{1}{2}\mathbf{C} : (\mathbf{A}(t + \Delta t) - \mathbf{I})$ using Eqs. (14) and (15)
    ii. Evaluate the trial RSS $\tau^\alpha = \mathbf{S}^{tr} : \mathbf{s}_0^\alpha$ and update deformation variables in step **B**.
    iii. From Eq. (14), obtain the starting iterate $\mathbf{S}^1(t + \Delta t) = \mathbf{S}^{tr} - \sum_\alpha \Delta\gamma^\alpha(t + \Delta t)\mathbf{C}^\alpha$
    iv. For the ith iteration in the Newton–Raphson algorithm
      (a) Evaluate $\tau^{i\alpha} = \mathbf{S}^i(t + \Delta t) : s_0^\alpha$ and update deformation variables in step **B**.
      (b) Using Eqs. (15) and (16), evaluate $\mathbf{S}^{i+1}(t + \Delta t) = \mathbf{S}^i(t + \Delta t) - \mathbf{d}_i^{-1}\mathbf{G}_i$ where $\mathbf{d}^i = \mathbf{I} + \sum_\alpha \mathbf{C}^\alpha \otimes \frac{\partial \Delta\gamma^{i\alpha}(t+\Delta t)}{\partial \mathbf{S}^i(t+\Delta t)}$ $\mathbf{G}_i = \mathbf{S}_i(t + \Delta t) - \mathbf{S}^{tr} + \sum_\alpha \Delta\gamma^\alpha(t + \Delta t)\mathbf{C}^\alpha$
      (c) Verify convergence: If no go to step (a); if yes go to step iv.
    v. Evaluate $\tau^\alpha = \mathbf{S}^{i+1}(t + \Delta t) : \mathbf{s}_0^\alpha$ and update deformation variables in item **B**.
    vi. From Eq. (13), evaluate $\mathbf{F}^p(t + \Delta t) = \{\mathbf{I} + \sum_\alpha \Delta\gamma^\alpha(t + \Delta t)\mathbf{s}_0^\alpha\}\mathbf{F}^p(t)$
    vii. Calculate $\mathbf{F}^e(t + \Delta t) = \mathbf{F}(t + \Delta t)\mathbf{F}^{p^{-1}}(t + \Delta t)$, $\boldsymbol{\sigma}(t + \Delta t) = \frac{1}{\det(\mathbf{F}^e(t+\Delta t))}\mathbf{F}^{eT}(t + \Delta t)\mathbf{S}(t + \Delta t)\mathbf{F}^e(t + \Delta t)$ and $\mathbf{W} = \frac{\partial \boldsymbol{\sigma}}{\partial \boldsymbol{\varepsilon}}$

B. Update deformation variables at any Stage

    I. Calculate dislocation density increments $\dot{\rho}_{SSD}^\alpha, \dot{\rho}_{GNDs}^\alpha, \dot{\rho}_{GNDet}^\alpha, \dot{\rho}_{GNDen}^\alpha$ from Eqs. (7) and (8)
    II. Evaluate ρ_P, ρ_F from Eq. (9) and ρ_m using Eq. (10).
    III. For activation of APB shearing, if: $\tau^\alpha > \tau_c$ and $\rho_m^\alpha > \rho_c$ in Eq. (11) then

      • Calculate $\tau_{pass}^\alpha, \tau_{cut}^\alpha$ for γ/γ' phases from Eq. (5) and $\dot{\gamma}^\alpha, \frac{\partial \dot{\gamma}^\alpha}{\partial \tau^\alpha}$ from Eq. (4) Otherwise
      • Calculate $\tau_{pass}^\alpha, \tau_{cut}^\alpha$ and then $\dot{\gamma}^\alpha, \frac{\partial \dot{\gamma}^\alpha}{\partial \tau^\alpha}$ only for γ phase.

Fig. 2. Comparing CPFEM results with those for tension experiments under a constant strain rate 0.0001 s^{-1}: (a) FEM mesh for cubic precipitates with the volume fraction of 70% and edge length 0.5 μm and (b) volume-averaged Cauchy stress-true (logarithmic)strain response.

Table 3
Experimentally calibrated parameters for the sub-grain scale crystal plasticity model.

Constant	c_1	c_2	c_3	c_4	c_5	c_6	c_7	τ_c	ρ_c
Value	4.0	0.8	1.0×10^{-3}	1.0×10^{-4}	10.0	10.0	0.3	110 MPa	1.0×10^{11}

Table 4
Stiffness and crystal plasticity parameters for the sub-grain model.

Phase	$C_{11} = C_{22} = C_{33}$	$C_{44} = C_{55} = C_{66}$	$C_{12} = C_{13} = C_{23}$	b	Q
γ	201.7 GPa	104.5 GPa	134.4 GPa	2.49 nm	$6.5 \times 10^{-19} J$
γ'	229.7 GPa	110.1 GPa	153.2 GPa	2.49 nm	$6.5 \times 10^{-19} J$

shapes of the γ' phase. The γ-channel-width l_c and shapes can vary significantly from point to point in the actual alloy. To explore the effect of γ channel-width only, two microstructures are constructed for comparison as shown in Fig. 3(a); one with non-symmetrical ($l_{c1} \neq l_{c2}$) γ' channel-width $l_{c1} = 0.069 \mu$m and $l_{c2} = 0.139 \mu$m, and the other with symmetric channel-width, i.e., $l_{c1} = l_{c2} = 0.122 \mu$m. The volume fraction of cubic γ' precipitates in both the microstructures is 35%. Simulations are conducted for a constant tensile strain-rate of 5×10^{-5} s^{-1} in the y-direction, corresponding to the [0 1 0] slip direction. The stress–strain response in Fig. 3(b) exhibits some difference in plastic response, with higher hardness for the non-symmetrical RVE.

2.5. Effect of γ' APB shearing and precipitate shape on the overall response

Fig. 4 plots the volume-averaged stress–strain response by CPFEM simulations for the RVE in the previous section, with and without the activation of APB shearing of γ' precipitates. The figure also shows the response for only the γ phase. In the absence of the γ' phase, the overall yield strength as well the hardening are considerably low. The alloy gets its high yield stress and hardening behavior from the γ' phase in the matrix. The stress–strain response is rather stiff if the APB shearing mechanism is not activated in the high volume fraction ($\sim$70%) γ' phase that has zero initial dislocation density. The accumulation of dislocation density at the $\gamma - \gamma'$ phase interfaces with high stresses leads to APB shearing, with super-dislocations entering the γ'-phase and softening the overall response. Accurate representation of the stress–strain response requires incorporation of the APB shearing criteria and associated relations for plastic flow in the γ'- phase.

Three different stages of deformation are marked by points in the stress–strain response of Fig. 5(a). For deformation up to state-point 1, both γ and γ' phases behave elastically and there is no plastic deformation in the domain. From state 1 to state 2, the γ-phase experiences plastic deformation and SSDs start to evolve, with plastic strain gradient building especially near the $\gamma - \gamma'$ interfaces. To preserve lattice continuity, the GNDs must evolve causing an increase in mobile dislocation density ρ_m. The distribution of ρ_m along the x-axis at state 2 is plotted in Fig. 5(b). There is little difference in ρ_m for the states 1 and 2 in the γ' phase. However this difference is significant in the γ-channel due to evolution of GNDs. In the post APB shearing stage, the γ'-phase experiences plastic deformation with considerable rise in ρ_m. Fig. 5(c) and (d) show the ρ_m distribution at states 2 and 3. At state 2, corresponding to the activation of APB shearing, the initial value of ρ_m does not change in the γ' phase. Beyond this state, ρ_m starts to evolve and reaches the distribution in Fig. 5(d) at 5% strain.

The effect of precipitate shape is explored through another RVE containing a 40% volume fraction of spherical precipitates as shown in Fig. 6(a). The channel width for spherical precipitates is the same as for cubic at the boundary, but increases at other regions. This corresponds to a precipitate radial edge-length of 0.45 μm. All other conditions are the same as in the constant strain-rate problem of the previous example. The microstructural RVE model is discretized into 1512, 8-noded brick elements. The same state-markers are inserted in stress–strain response plot of Fig. 6(b). The distributions of the mobile dislocation density at states 1, 2 and 3 along the x-axis are plotted in Fig. 6(c), while Fig. 6(d) shows the ρ_m distribution at state 3. Responses for the cubic and spherical precipitates are quite different between the states 1 and 2. For the cubic shape, the transition of plastic flow from the γ to γ' phase is sharp. Plastic deformation in the γ channel does not affect the response much, as the channel
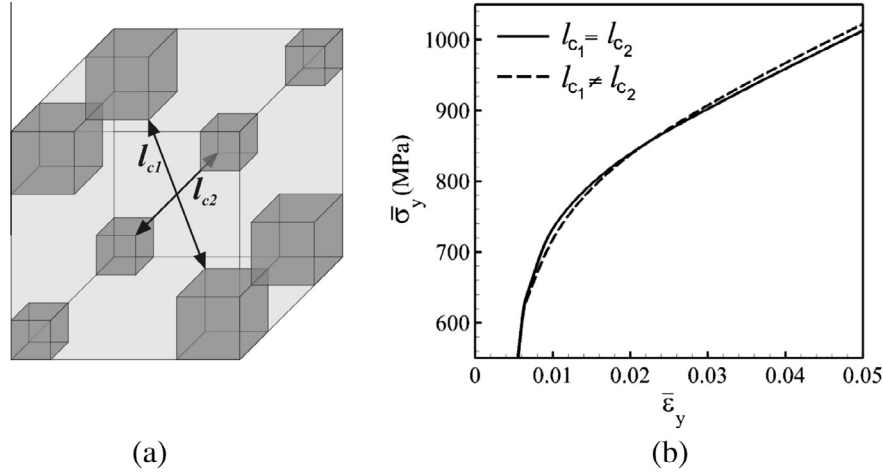
(a)

(b)

Fig. 3. (a) RVE with non-symmetric diagonal channel widths and (b) comparison of Cauchy stress-true strain response under tension constant strain rate 0.005% for cubic precipitates with the same volume fraction 35% and RVE size (0.24 μm).
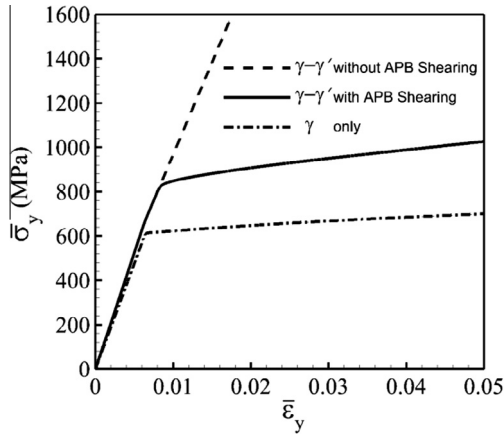

Fig. 4. The effect of activation of APB shearing on stress strain curve under tension constant strain rate at 800 °C.

width is generally small as observed in Fig. 2(a). This situation is different for the spherical precipitates where after state 1, nucleated dislocations in the γ phase rapidly evolve in the channel where the round interface between γ and γ' provides more spaces to accommodate higher dislocation densities.

3. Grain-scale crystal plasticity model with microtwinning

3.1. Homogenized activation energy-based crystal plasticity (AE-CP) model

Results of simulation of the sub-grain RVE model, discussed in Section 2, are homogenized to generate constitutive parameters for a grain-scale activation energy-based crystal plasticity (AE-CP) model. Determination of parameters is assumed to be governed by the Hill–Mandel principle of macro-homogeneity (Hill, 1984; Nemat-Nasser, 1999), expressed as:

$$\langle \boldsymbol{S} \rangle : \langle \dot{\boldsymbol{E}} \rangle = \frac{1}{\Omega_{RVE}} \int_{\Omega_{RVE}} \boldsymbol{S} \mathrm{d}V : \frac{1}{\Omega_{RVE}} \int_{\Omega_{RVE}} \dot{\boldsymbol{E}} \mathrm{d}V = \frac{1}{\Omega_{RVE}} \int_{\Omega_{RVE}}$$

$$\boldsymbol{S} : \dot{\boldsymbol{E}} \mathrm{d}V = \langle \boldsymbol{S} : \dot{\boldsymbol{E}} \rangle \qquad (17)$$

Here $\boldsymbol{S}$ and $\dot{\boldsymbol{E}}$ correspond to the second Piola–Kirchhoff stress and the Lagrangian strain rate, respectively and the symbol $\langle \bullet \rangle$ corresponds to volume averaging over the RVE domain. The constitutive parameters are formulated in terms of morphological variables and are calibrated by computational homogenization.

The proposed grain-scale, homogenized crystal plasticity model for *fcc Ni*-based superalloys follows the framework of activation energy-based crystal plasticity (AE-CP) models (Kocks et al., 1975; Frost and Ashby, 1982; Xie et al., 2004). The homogenized constitutive model incorporates an evolving thermal shear resistance as well as an athermal shear resistance due to plastic deformation. For a slip system α, the plastic shearing rate follows from the Orowan equation as:

$$\dot{\gamma}^{\alpha} = \begin{cases} 0 \text{ if } \tau_{eff}^{\alpha} \leqslant 0 \\ \dot{\gamma}_{*}^{\alpha} \exp\{-\frac{Q}{k_B \theta}(1 - [\frac{|\tau_{eff}^{\alpha}|}{s_{*}^{\alpha}}]^p)^q\} \mathrm{sgn}(\tau^{\alpha}) \text{ if } 0 \leqslant \tau_{eff}^{\alpha} \leqslant s_{*}^{\alpha} \end{cases} \qquad (18)$$

Here Q is the activation energy barrier, $k_B (= 1.3807 \times 10^{-23} \mathrm{J\,K^{-1}})$ is the Boltzmann's constant, θ is the temperature and exponents p, q are material constants. For the slip system α, $\dot{\gamma}_{*}^{\alpha}$ is a reference strain-rate, $\tau_{eff}^{\alpha} (= |\tau^{\alpha}| - s_{a}^{\alpha})$ is the effective resolved shear stress. The temperature-dependent critical slip resistance $s^{\alpha} (> 0)$ is assumed to be comprised of a thermally activated obstacle to slip s_{*}^{α} and a part due to the athermal obstacles s_{a}^{α}. The athermal and thermal shear resistances s_{a}^{α} and s_{*}^{α} correspond to the passing and cutting stress barriers, respectively. The difference between the athermal shear resistance and the resolved shear stress is the driving force for dislocation motion on the slip system α. $\dot{\gamma}_{*}^{\alpha}$ can evolve with the activation of APB shearing, when the γ-phase experiences plastic deformation with increasing dislocation density, especially near the $\gamma - \gamma'$ interfaces. This deformation effect can be significant for some γ' precipitate shapes, e.g., spherical, but not as strong for cuboidal. An yield point phenomenon is applied to introduce a morphology dependent functional form for $\dot{\gamma}_{*}^{\alpha}$ (Keshavarz and Ghosh, 2013) as:

$$\dot{\bar{\gamma}} = H(\bar{\varepsilon}_p - l_p) \dot{\gamma}_0 \left\{ \frac{\tanh(k) + \tanh(kl_p)}{10 \left\{ \tanh[\bar{k}(\bar{\varepsilon}_p - l_p)] + \tanh(kl_p) \right\}} - 1 \right\} + \dot{\gamma}_0 \qquad (19)$$

where H is the Heaviside step function, $\dot{\gamma}_0$ corresponds to the initial strain rate and l_p, k, k_* are material constants. In this work $l_p = 10^{-4}$ and k and k_* are derived in terms of morphological parameters. The equivalent plastic strain $\bar{\varepsilon}_p (= \sqrt{\frac{2}{3} \varepsilon_{ij}^p \varepsilon_{ij}^p})$ is defined in terms of the Lagrangian plastic strain $\varepsilon_{ij}^p = \frac{1}{2}(F_{ij}^{pT} F_{ij}^p - \delta_{ij})$. Consequently, evolution laws for thermal and athermal shear resistances, contributing to the overall slip resistance s^{α}, are proposed in terms of the plastic strain
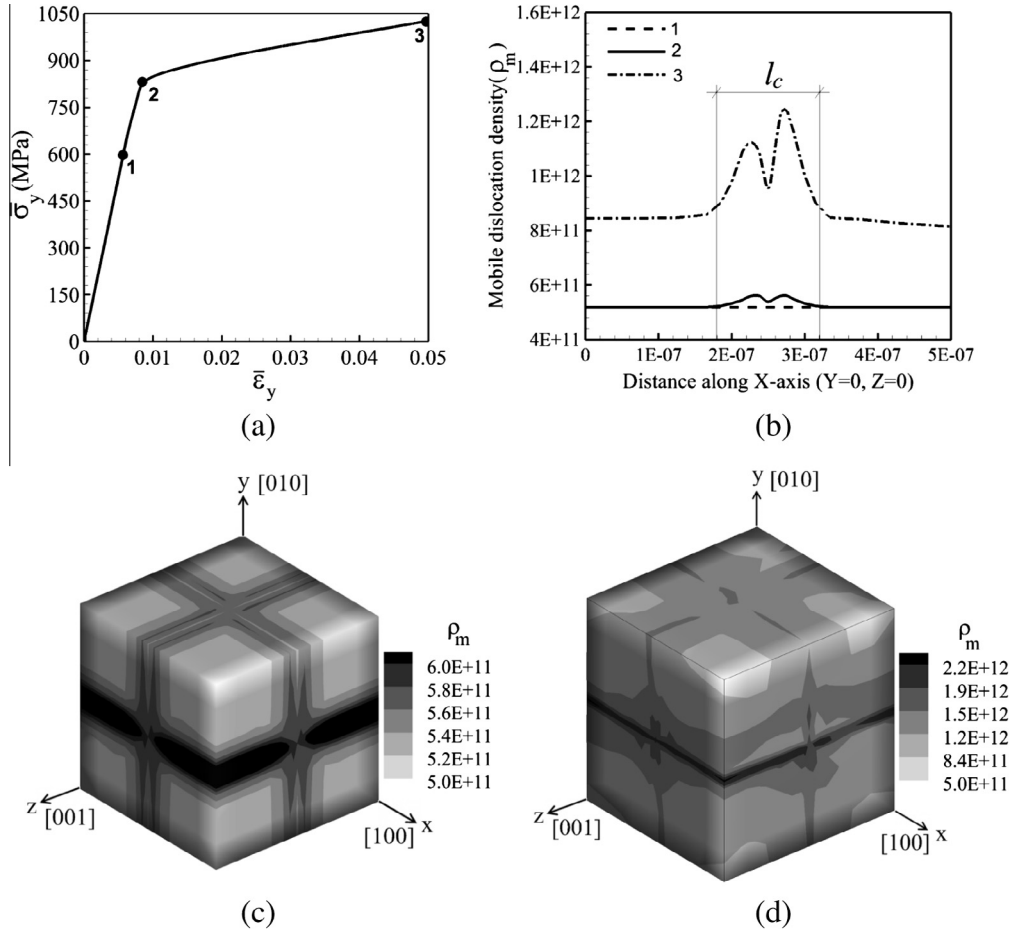
Fig. 5. Effect of APB shearing for RVE with cubic γ' precipitates: (a) stress–strain response with three state-markers, (b) distribution of mobile dislocation density along X-axis for the three states, and (c,d) mobile dislocation density contour plots at states 2 and 3, respectively.

rate. The thermal shear resistance, accounting for forest dislocations normal to the slip plane and the athermal shear resistance reflecting the effect of parallel dislocations in the slip direction m^α, are expressed as:

$$\dot{s}_a^\alpha = \sum_{\beta=1}^n h_a^{\alpha\beta} |\dot{\gamma}^\beta \sin(\mathbf{n}_\alpha, \mathbf{t}^\beta)|, \quad \dot{s}_*^\alpha = \sum_{\beta=1}^n h_*^{\alpha\beta} |\dot{\gamma}^\beta \cos(n_\alpha, t^\beta)| \quad (20)$$

where $\mathbf{n}_\alpha$ is slip-plane normal, $\mathbf{t}_\alpha = \mathbf{m}^\alpha \times \mathbf{n}_\alpha$, and the total shear resistance is $\dot{s}^\alpha = \sqrt{(\dot{s}_a^\alpha)^2 + (\dot{s}_*^\alpha)^2}$. The initial values of the athermal and thermal shear resistances are respectively $s_{a0}^\alpha, s_{*0}^\alpha$. For convenience, coefficients accounting for the interactions between slip systems are taken to be the same i.e., $h_a^{\alpha\beta} = h_*^{\alpha\beta} = h^{\alpha\beta}$. Each component of $h^{\alpha\beta}$ is the deformation resistance on slip system α due to shearing on slip system β. It describes both self and latent hardening as:

$$h^{\alpha\beta} = q^{\alpha\beta} h^\beta, \quad \text{where} \quad h^\beta = \left[h_0 \left(1 - \frac{s^\beta}{s_{sat}^\beta}\right)^r \right] sign\left(1 - \frac{s^\beta}{s_{sat}^\beta}\right) \quad (21)$$

The parameter h^β denotes the resistance dependent self-hardening rate, s_{sat}^β is the saturation value of reference shear stress and r is a constant exponent. The coefficient $q^{\alpha\beta} = q + (1 - q)\delta^{\alpha\beta}$, where q is a latent-hardening parameter chosen as 1.4.

3.1.1. Sub-grain morphological parameters

Three characteristic parameters representing the sub-grain microstructural morphology in Fig. 1(c), are delineated as: (i) γ' volume fraction v_p, (ii) γ' shape factor n, and (iii) minimum limiting

channel-width l_c between γ' precipitates. The volume fraction is expressed as the ratio of the γ' precipitate volume to the RVE volume, i.e., $v_p = \frac{\Omega_{\gamma'}}{\Omega_{RVE}}$. The shape factor is described in terms of the exponent of a generalized ellipsoid: $\left(\frac{x}{a}\right)^n + \left(\frac{y}{b}\right)^n + \left(\frac{z}{c}\right)^n = 1$, where a, b and c are the dimensions of the three principal axes and n is shape exponent. Here, $a = b = c$ is assumed to represent equiaxed precipitates. A value $n = 2$ corresponds to a sphere while $n \to \infty$ corresponds to a cube. To avoid a singular value of n, a transformed shape factor $n_1 = \tan^{-1}(n)$ is used in the parameterization.

The effect of these morphological parameters on the volume-averaged stress–strain response of the RVE using the sub-grain dislocation density CPFE simulations is examined and depicted in Fig. 7. For each simulation conducted at 0.0001 s^{-1} and 800 °C, one of the parameters is varied, while the other two are held constant. Variables considered are (i) cubic precipitates of volume fractions 75.13% and 57.87%, (ii) shape factors $n = 2.0$ and ∞, and (iii) channel-width $l_c = 0.29$ μm and $l_c = 0.58$ μm for cubic precipitates of 29.63% volume fraction. Results in Fig. 7 show that with increasing volume fraction, the post-yield plastic response does not change too much even though the yield strength increases. The yield strength changes and the plastic response diverges with increasing strain for different shapes. The plastic response changes with increasing channel-width, while the yield strength decreases only slightly.

Plastic slip and hardening parameters in the grain-scale AE-CP model are functions of the SSDs and GNDs. SSDs do not generally change much with morphological variables i.e. they are size inde-
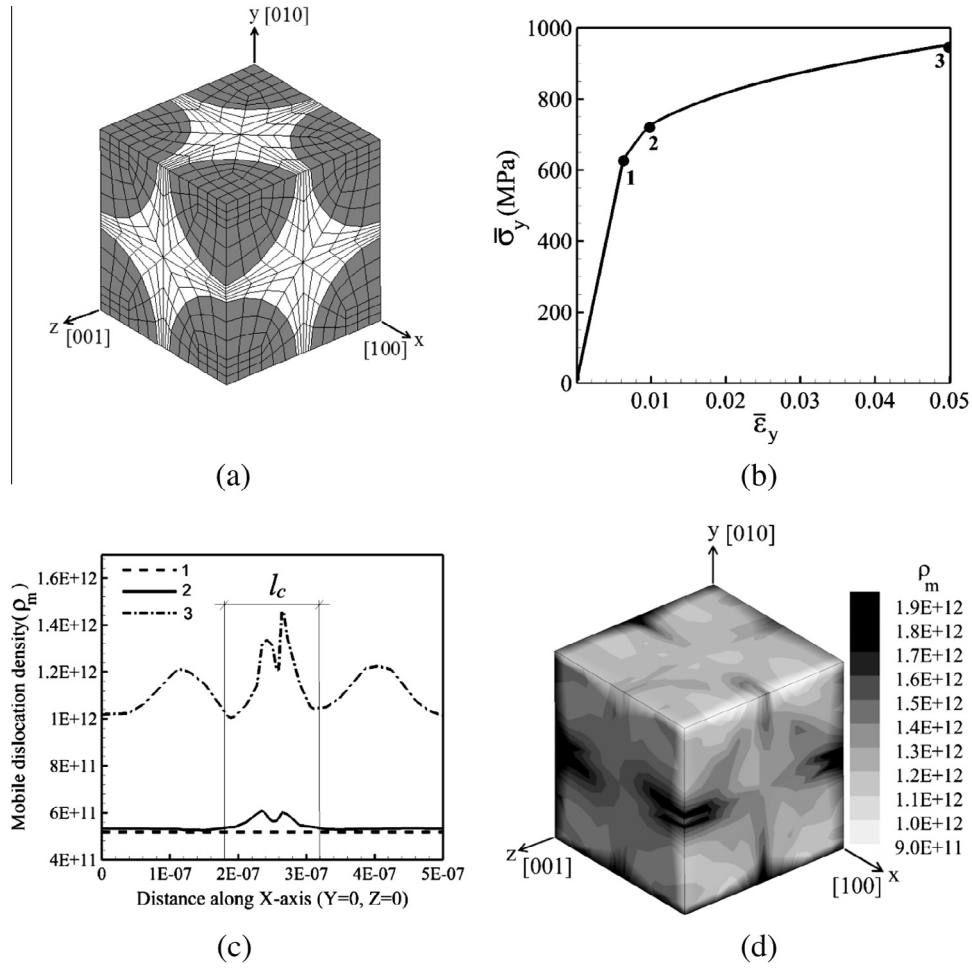
Fig. 6. Effect of APB shearing for RVE with spherical γ' precipitates: (a) CPFEM mesh, (b) stress–strain response with three state-markers, (c) distribution of mobile dislocation density along X-axis for the three states, and (d) mobile dislocation density contour plot at state 3.

pendent, but GNDs can vary significantly with precipitate shape and size. Forest and parallel components of dislocation densities may be expressed as:

$$\rho_F(\rho_{SSD}, \rho_{GND}) = \rho_F(\gamma^\alpha, \nabla\gamma^\alpha), \quad \rho_P(\rho_{SSD}, \rho_{GND}) = \rho_P(\gamma^\alpha, \nabla\gamma^\alpha) \quad (22)$$

Crystal plasticity hardening parameters are functions of the plastic slip γ^α due to SSD's. Morphological parameters should also be incorporated in these functions to account for the effect of GNDs or gradient of plastic shear strain $\nabla\gamma^\alpha$. Sensitivity analyses indicate that the initial thermal shear resistance and its rate, the reference slip-rate $\dot{\gamma}_*$ and the saturation shear stress s_{sat}^a are functions of the morphology. Thus, in Eqs. (19)–(21) parameters $\dot{s}_*^\alpha(n_1, v_p, l_c)$, $\dot{\gamma}_*(n_1, v_p, l_c)$, $s_{sat}^\alpha(n_1, v_p, l_c)$, are derived in terms of morphological parameters as well as $(\gamma^\alpha, \nabla\gamma^\alpha)$ as:

$$\dot{s}_*^\alpha(n_1, v_p, l_c) = \sum_{\beta=1}^{n} h^{\alpha\beta}(n_1, v_p, l_c)|\dot{\gamma}^\beta \cos(n_\alpha, t^\beta)|$$

$$= \sum_{\beta=1}^{n} \left[h_0 \left(1 - \frac{s^\beta}{s_{sat}^\beta(n_1, v_p, l_c)} \right)^r \right] \text{sgn}$$

$$\times \left(1 - \frac{s^\beta}{s_{sat}^\beta} \right) |\dot{\gamma}^\beta \cos(n_\alpha, t^\beta)| \quad (a)$$

$$\dot{\gamma}_*(n_1, v_p, l_c) = H(\bar{\varepsilon}_p - l_p)\dot{\gamma}_0$$

$$\left\{ \frac{\tanh[k(n_1, v_p, l_c)] + \tanh[k(n_1, v_p, l_c)l_p]}{10\{\tanh[k_*(n_1, v_p, l_c)(\bar{\varepsilon}_p - l_p)] + \tanh[k(n_1, v_p, l_c)l_p]\}} - 1 \right\} + \dot{\gamma}_0 \quad (b)$$

$$(23)$$

The initial strain rate $\dot{\gamma}_0$ and hardening parameter h_0 are insensitive to the morphology.

3.1.2. Calibrating the grain scale AE-CP model parameters

Eqs. (18)–(21) and (23) contain a number of material parameters, some of which vary with the morphology while others are independently constant. The constant material parameters that should be experimentally calibrated for the AE-CP model are the activation energy Q and exponents p, q in Eq. (17), $\dot{\gamma}_0$ in Eq. (18) and hardening parameter h_0 and exponent r in Eq. (20). These parameters have been calibrated in Keshavarz and Ghosh (2013) for single crystal CMSX-4 using experimental data from tensile constant strain-rate and creep tests in Knowles and Gunturi (2002) and Fleury et al. (1996), respectively. The parameters are listed in Table 5.

Subsequently, the morphology-dependent AE-CP parameters $s_{*0}^\alpha(n_1, v_p, l_c)$, $k_*(n_1, v_p, l_c)$, $k(n_1, v_p, l_c)$ and $s_{sat}^\beta(n_1, v_p, l_c)$ in Eq. (23) are calibrated from the simulated volume-averaged response of the sub-grain RVE model. These simulations are conducted under a constant strain-rate of $0.0001\,\text{s}^{-1}$ in the [010] direction at 800 °C. The calibration process has involved 37 different RVE microstructures, as follows:

   i. 4 microstructures with $n = 1.5$, v_p and 4 different $l_c's$;
   ii. 16 microstructures with $n = 2.0$, $v_p = 0.1065, 0.1544$, 0.3016 and 0.3916, and 4 different $l_c's$;
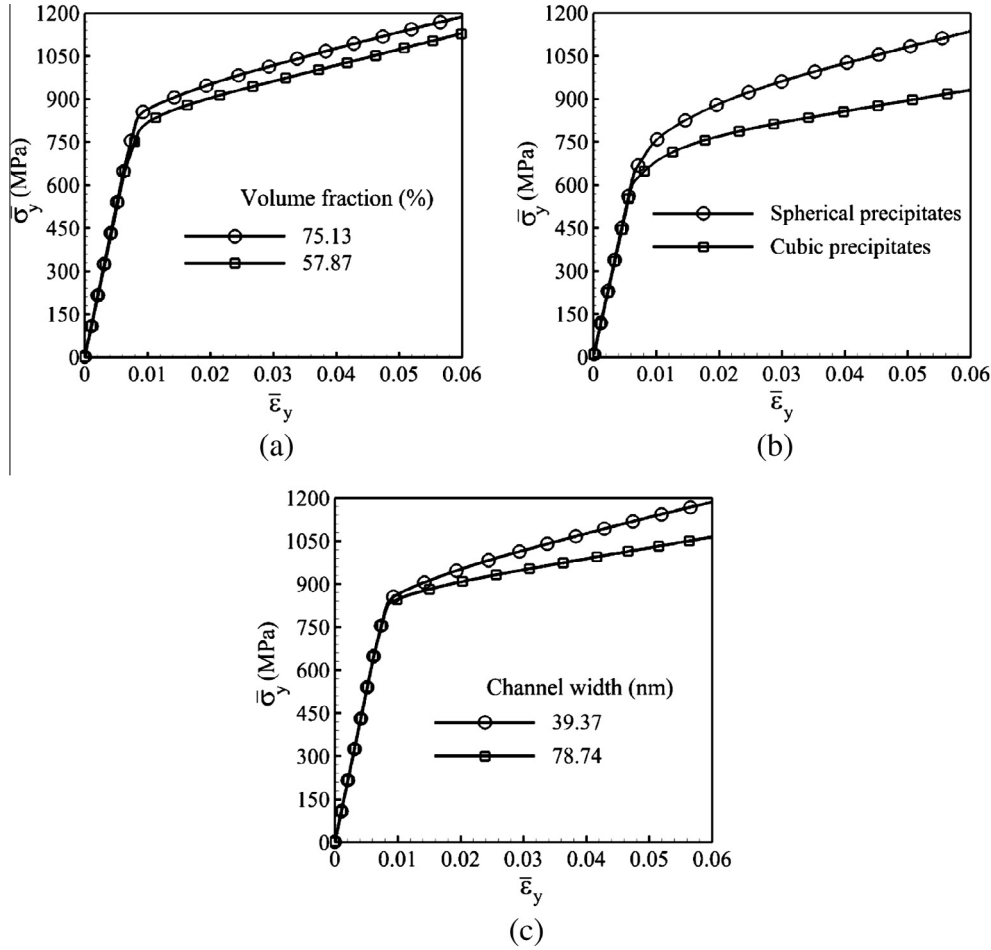
Fig. 7. Effect of γ' precipitate (a) volume fraction, (b) shape, and (c) channel width for cubic precipitates with 29.63% volume fraction, on the stress–strain response under constant tensile strain-rate of 0.0001 s⁻¹ at a temperature of 800 °C.

iii. 16 microstructures with $n = 4.27$, $v_p = 0.1043, 0.2474$, $0.4832, 0.6273$ and 4 $l'_c s$;

iv. a microstructure with $n \to \infty$.

An example of the sub-grain RVE, FE model containing spherical precipitates of 39.16% volume fraction and different channel-widths, discretized into 8-noded brick elements, is depicted in Fig. 8(a). In Fig. 8(b), the homogenized AE-CP model parameters are calibrated with the averaged stress–strain responses from the RVE model.

3.1.3. Functional forms of homogenized AE-CP constitutive parameters

Functional forms of the constitutive parameters $s^\alpha_{*0}(n_1, v_p, l_c)$, $k_*(n_1, v_p, l_c)$, $k(n_1, v_p, l_c)$ and $s^\beta_{sat}(n_1, v_p, l_c)$ in Eqs. (23) are generated for representing the effect of morphology on the single crystal behavior. To derive these functional forms by computational homogenization, a large number of sub-grain RVE model simulations with varying volume fractions, channel-widths and shapes are conducted (Keshavarz and Ghosh, 2013). These set of simulations yield the following functional forms, where the coefficients are determined by solving a set of least square minimization problems.

(I) $\quad s^\alpha_{*0}(n_1, v_p, l_c) = a_1(n_1, v_p) + \dfrac{b_1(n_1, v_p)}{\sqrt{l_c}}$

$$= 1039 + 559v_p - 99n_1 - 136v_pn_1$$

$$+ \frac{-0.1 + 89v_p + 53n_1 - 90v_pn_1}{\sqrt{l_c}} \qquad (24)$$

(II) $\quad s^\alpha_{sat}(n_1, v_p, l_c) = a_2(n_1, v_p) + \dfrac{b_2(n_1, v_p)}{l_c}$

$$= 3185 - 8905v_p - 1648n_1 + 6680v_pn_1$$

$$+ \frac{-0.21 + 5008v_p + 363n_1 - 3599v_pn_1}{l_c}$$

$$(25)$$

(III) $\quad k_*(n_1, v_p, l_c) = 65 - 7500v_p + 33n_1 - 2700l_c$

$$+ 12768v_pn_1 - 23120v_pl_c + 4080n_1l_c$$

$$- 19847v_pn_1l_c \qquad (26)$$

(IV) $\quad k(n_1, v_p, l_c) = a_3(n_1, v_p) + \dfrac{b_3(n_1, v_p)}{\sqrt{l_c}}$

$$= 5.5 - 327.6v_p + 31.5n_1 + 221.4v_pn_1$$

$$+ \frac{0.14 + 281.2v_p - 2.44n_1 - 176.5v_pn_1}{\sqrt{l_c}} \qquad (27)$$

The explicit dependence on channel-width l_c reflects the size-effect due to the presence of GNDs in the sub-grain dislocation density CP model. In Eqs. (24)–(27) the unit of l_c is μm, while the units of initial thermal resistance and saturation shear resistance in Eqs. (24) and (25) are *MPa*.
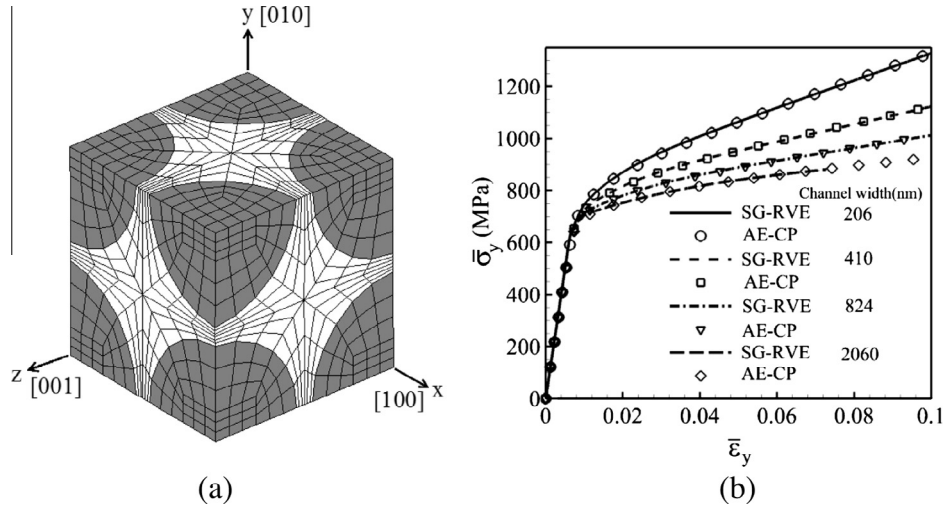
Fig. 8. Calibration of morphology-dependent homogenized crystal plasticity parameters in the grain-scale activation energy-based crystal plasticity (AE-CP) model: (a) FEM model of the sub-grain RVE (SG-RVE) with spherical precipitates of volume fraction 39.16% and (b) stress–strain response by the SG- RVE and AE-CP FE models.

Table 5
Experimentally calibrated constant material parameters for the grain scale AE-CP model.

Parameters	Q (J)	p	q	$\dot{\gamma}_0$ (s^{-1})	h_0 (MPa)	r
Value	6.5×10^{-19}	0.78	1.15	5.0×10^{7}	1300	1.115

3.1.4. Validation of the homogenized AE-CP model

Two sets of validation tests are conducted for the homogenized AE-CP constitutive model. In the first set, the results of a single grain, crystal plasticity FEM analysis with the calibrated homogenized AE-CP constitutive model are compared with the averaged response of a sub-grain RVE (SG-RVE) analysis. Three cases, corresponding to different microstructures, are considered for simulation. These are:

Case 1 : $n = 10$, $v_p = 44\%$, $l_c = 0.135 \ \mu m$;
Case 2 : $n = 1.5$, $v_p = 22\%$, $l_c = 0.260 \ \mu m$;
Case 3 : $n = \infty$, $v_p = 30\%$, $l_c = 0.576 \ \mu m$,

Simulations for both the AE-CP and SG-RVE FE models are conducted for an applied strain-rate of 0.0001 s^{-1} in the y-direction at 800 °C. The true stress- logarithmic strain response by the AE-CPFE model and the averaged stress–strain response by the SG-RVE FE model are plotted in Fig. 9. Excellent agreement is obtained between the homogenized grain-scale AE-CPFE model with morphological parameters and the explicit sub-grain RVE model. A notable advantage of the homogenized model is the significant efficiency gain over explicit RVE models. For this example, the gain in efficiency is of the order of 10^4 (few seconds for AE-CPFE model) with identical response. This efficiency advantage is necessary when modeling polycrystalline microstructures.

The second example involves validating the AE-CP constitutive model with results from creep experiments in (Ma et al., 2008) for single crystal CMSX-4 with 70% volume fraction of γ' precipitates. In Ma et al. (2008) two tensile loads of 650 and 770 MPa are applied in the [0 0 1] direction at 750 °C. CPFEM analyses with the homogenized parameters are conducted for a single grain under these conditions. The simulated logarithmic strain–time response by the simulations is compared with the experimental results in Fig. 10 with good agreement.

3.2. Micro-twinning in grain-scale crystal plasticity model: tension–compression asymmetry

Single crystal experiments on *Ni*-based superalloys show considerable tension–compression asymmetry. Large difference in the creep response for single crystals loaded in the [0 0 1] and [0 1 1] directions under tension and compression conditions has been reported in Fleury et al. (1996) and Knowles and Gunturi (2002). APB shearing is responsible for the difference in tension and compression tests in the [0 0 1] direction. However, transmission electron microscopy observations in Unocic et al. (2011) have reported micro-twinning mechanism for high temperature creep deformation. To account for this tension–compression asymmetry, a microtwinning model developed in Unocic et al. (2011) is incorporated in the grain-scale crystal plasticity formulation. The criterion for micro-twin nucleation in Unocic et al. (2011) is based on the state of dissociation of the leading and trailing partials on a slip system, where the condition for dissociation of a full dislocation $a/2\langle 110 \rangle$ is given as a function of the magnitude and orientation of the in-plane shear stress. With deformation, the leading and trailing Shockley partials experience stresses τ_{lead} and τ_{trail} respectively. From the magnitudes of in-plane resolved shear stress $\tau^{inplane}$, stresses τ_{lead} and τ_{trail} the criterion examines whether the partials will remain together or get dissociated at the interface of the $\gamma - \gamma'$ phases. Thus, if $\|\tau^{inplane}\| > \tau_{lead} \|\tau^{inplane}\| < \tau_{trail}$, the leading partial passes through and hence the leading and trailing partials remain dissociated. The direction of dislocation is also another determinant for dissociation. This condition is applied to yield asymmetry due to the difference in the direction of dislocation motion for tension and compression.

The micro-twin evolution model is based on the premise that γ' precipitate shearing and subsequent re-ordering is the predecessor to the movement of partials that cause plastic slip. The thermal re-ordering rate by diffusion depends on the activation energy barrier, i.e. $R_{reorder} \propto \exp\left(-\frac{\Delta E + p\Delta V_{act} - \theta \Delta S}{k_B \theta}\right)$, where ΔE is the internal energy barrier, p is the pressure, ΔV_{act} is the activation volume for pressure dependent diffusion, ΔS is the change in entropy, k_B is Boltzmann's constant and θ is the absolute temperature. For solids, the pressure dependent activation volume ΔV_{act} is small and is hence ignored. Change in entropy occurs due to irreversible dissipation such as plastic work and is expressed as: $\theta \Delta S = W_p = \tau_{eff} A_p b_{tp}$, where τ_{eff} is the effective shear stress, A_p is the shearing area during plastic
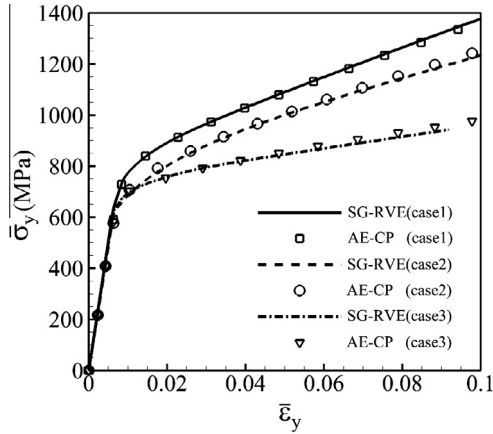
Fig. 9. Validation of the homogenized grain-level activation energy-based crystal plasticity (AE-CPFE) model with a FEM model of the sub-grain RVE (SG-RVE) for three different microstructures.
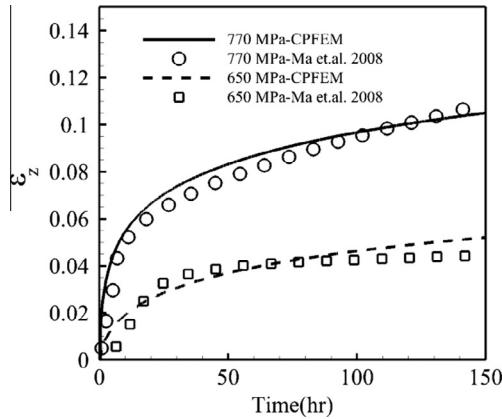

Fig. 10. Creep response by the homogenized AE-CP FEM and experiments in (Ma et al., 2008) for tension tests in [001] direction with 750 MPa and 650 MPa, respectively at 750 °C.

deformation and b_{tp} is the Burgers vector of the twin partials. The velocity of twin partials may be written as:

$$v_{tp} = f_{reorder} \lambda_{reorder} P_{reorder}(\Delta E, \theta \Delta S) \qquad (28)$$

where $f_{reorder}$ is the frequency of re-ordering, $\lambda_{reorder}$ is the reordering distance and $P_{reorder}$ is the probability of re-ordering against the energy barrier, which is a function of plastic dissipation and internal energy barrier. The internal energy barrier is expressed as $\Delta E = \Gamma(t) A_{eff}$, where $\Gamma(t) = (\Gamma_{pt} - \Gamma_{tt}) \exp(-Kt) + \Gamma_{tt}$ is the energy drop, which decreases exponentially with time from pseudo-twin energy Γ_{pt} to true twin energy Γ_{tt}. The effective shear stress including the effect of tertiary γ' precipitates is expressed in Karthikeyan et al. (2006) as $\tau_{eff} = \tau - \frac{f_3}{2} \frac{\Gamma_{pt}}{b_{tp}}$, where f_3 is the volume fraction of the tertiary γ' precipitates. Thus, the plastic shear strain-rate due to micro-twinning is written from the Orowan equation as:

$$\dot{\gamma} = \rho_{tp} b_{tp} \lambda_{reorder} f_{reorder} \exp\left\{ -\frac{A_{eff} \Gamma(t) - V_{act} \tau_{eff}}{k_B \theta} \right\} \qquad (29)$$

where ρ_{tp} is the density of partials which is a function of applied stress and time.

The homogenized AE-CP model, along with the grain-scale micro-twin nucleation and evolution models in Eqs. (18)–(29), are employed to simulate creep response of single crystal superalloys. Significant tension–compression asymmetry is observed in

the experimental data plotted in Fig. 11 for single crystal CMSX-4 specimen (Kakehi, 1999). Micro-twin formation is not seen for tension loading in the [001] direction. However, significant micro-twin has been seen to develop for compression in this direction in the TEM studies of Kakehi (1999). Deformation is dominated by strain due to micro-twin evolution as shown in Fig. 11(a). Similar observations have also been made in experiments with loading in the [011] direction. For tensile and compressive creep tests, the observed trend shown in Fig. 11(b), is opposite to that for the [001] direction. Micro-twins in the deformed micro-structure are observed for tension loading in the [011] direction, whereas no micro-twin induced deformation is seen for compression loading. Results of compression creep experiments with single crystals containing 70% volume fraction of cubic precipitates (Fleury et al., 1996; Karthikeyan et al., 2006) are used to calibrate material constants in Eq. (29). For compression tests, the loading conditions and microstructures are the same as in the tensile tests of Section 3.1. Experimentally calibrated material constants are: $\rho_{tp} = 1.0e11 \text{ m}^{-2}$, $b_{tp} = 0.145 \, \mu\text{m}$, $\lambda_{reorder} = 0.3$, $f_{reorder} = 1.0$, $\Gamma_{pt} = 0.7 \text{ Jm}^{-2}$ and $\Gamma_{tt} = 0.02 \text{ Jm}^{-2}$. Results of CPFE simulations are compared with experimental data (Kakehi, 1999) in Fig. 11 for validation. The grain-scale crystal plasticity FE model satisfactorily predicts single crystal experimental data, including micro-twin induced tension–compression asymmetry.

4. Augmented AE-CP model for polycrystalline microstructures

Polycrystalline microstructures of Nickel-based superalloys are modeled in this section using the homogenized AE-CP model with parametric representation of the $\gamma - \gamma'$ microstructure, together with the micro-twin nucleation and evolution models. For modeling polycrystalline microstructures however, the AE-CP model should be modified to account for grain boundary lattice incompatibility. Hardening laws, accounting for GNDs, have been proposed to address lattice incompatibility in Acharya and Beaudoin (2000) using the Nye tensor along slip plane normal. In the present study, the dislocation density-based slip relations have been extended to take into account lattice incompatibility. The hardening parameters in Eq. (20) are augmented to account for lattice deformation incompatibility at grain boundaries due to plastic strain gradients leading to dislocation pileup. The athermal and thermal shear resistances in Eq. (20) are each divided into two parts, corresponding to SSDs and GNDs as:

$$s_a^\alpha = s_{a,SSD}^\alpha + s_{a,GND}^\alpha, \quad s_*^\alpha = s_{*,SSD}^\alpha + s_{*,GND}^\alpha \qquad (30)$$

where

$$s_{a,GND}^\alpha = \bar{c}_1 Gb \sqrt{\rho_{GP}^\alpha}, \quad s_{*,GND}^\alpha = \frac{Q}{\bar{c}_2 b^2} \sqrt{\rho_{GF}^\alpha} \qquad (31)$$

These relations are consistent with those in the sub-grain scale model in Eq. (5), where the cutting and passing shear resistances are expressed as functions of parallel and forest dislocation densities. In Eq. (31) $\bar{c}_1$ and $\bar{c}_2$ are material constants, and ρ_{GP}^α, ρ_{GF}^α are parallel and forest dislocation densities resulting from GNDs corresponding to Eq. (9). They may be written as:

$$\rho_{GP}^\alpha = \sum_{\beta=1}^{N} \chi^{\alpha\beta} [\rho_{GNDs}^\beta | \sin(\mathbf{n}_\alpha, \mathbf{m}^\beta)| + \rho_{GNDet}^\beta | \sin(\mathbf{n}_\alpha, \mathbf{t}^\beta)|$$
$$+ \rho_{GNDen}^\beta | \sin(\mathbf{n}_\alpha, \mathbf{n}^\beta)|]$$

$$\rho_{GF}^\alpha = \sum_{\beta=1}^{N} \chi^{\alpha\beta} [\rho_{GNDs}^\beta | \cos(\mathbf{n}_\alpha, \mathbf{m}^\beta)| + \rho_{GNDet}^\beta | \cos(\mathbf{n}_\alpha, \mathbf{t}^\beta)|$$
$$+ \rho_{GNDen}^\beta | \cos(\mathbf{n}_\alpha, \mathbf{n}^\beta)|] \qquad (32)$$
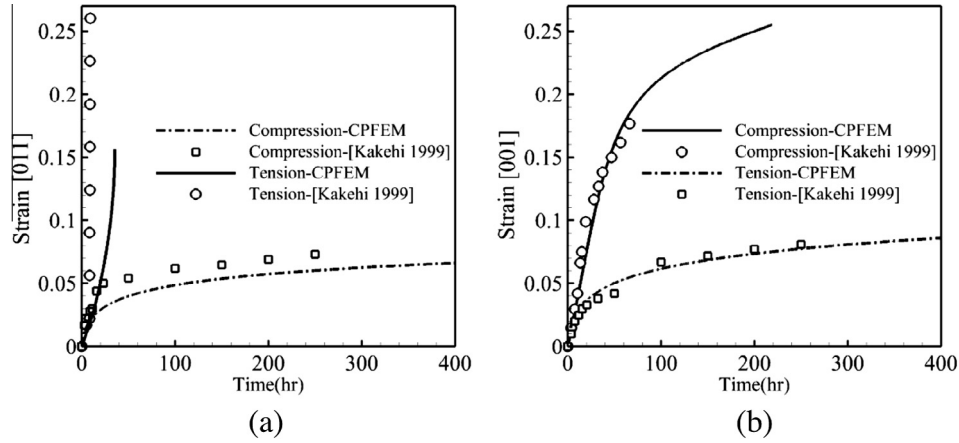
Fig. 11. Logarithmic strain–time response by the homogenized AE-CPFE model including micro-twin nucleation and evolution, with experimental data (Kakehi, 1999), for tension and compression creep in (a) [001] and (b) [011] directions.

where $\chi^{\alpha\beta}$ is the interaction strength coefficient and ρ_{GNDs}, ρ_{GNDet}, ρ_{GNDen} are a screw and two edge components of the GND densities respectively.

4.1. Implementation of GND based Hardness in the polycrystalline AE-CP model

As in Eq. (32), two sets of edge dislocation and one set of screw dislocation densities are required to calculate hardening parameters due to lattice incompatibility from Eq. (31). Different methods can be applied to calculate the plastic strain gradient for representing GND densities, in terms of the Nye's dislocation tensor Λ that quantifies dislocations over a volume which has geometric effects. It is divided into one screw and two edges components. In a component form Λ_{ij} refers to a set of dislocations with Burgers and tangent vectors along the i and j directions respectively. In (Arsenlis and Parks, 1999), it has been calculated as $\Lambda_{ij} = \frac{1}{V}\int_L b_i t_j ds$, where V is the volume over which the Nye tensor is calculated, L is the total length of the dislocation lines and ds refers to a differential segment along the dislocation line. Vectors $\mathbf{b}$ and $\mathbf{t}$ designate the Burgers and tangent vectors, respectively. Discretizing the dislocation lines into different groups with constant Burgers vector, the Nye tensor components can be written as:

$$\Lambda_{ij} = \frac{1}{V}\sum_\zeta b_i^\zeta \int_l t_j^\zeta ds^\zeta \approx \frac{1}{V}\sum_\zeta b_i^\zeta \sum_k \bar{l}_{(k)}^\zeta \bar{t}_{j(k)}^\zeta$$
$$= \sum_\zeta b_i^\zeta \sum_k \rho_{(k)GND}^\zeta \bar{t}_{j(k)}^\zeta \qquad (33)$$

Here l is the length of dislocation line of type ζ. For each dislocation line segment k in the discretized expression, the length and orientation of the line connecting the endpoints of the dislocation segment are respectively $\bar{l}_k^\zeta = \|\mathbf{x}_k^+ - \mathbf{x}_k^-\|$, $\bar{\mathbf{t}}_k^\zeta = \frac{\mathbf{x}_k^+ - \mathbf{x}_k^-}{\bar{l}_k^\zeta}$. The last equality in Eq. (33) comes from the fact that the dislocation density is denoted by the length of the dislocation line divided by the volume. The dislocation space should be discretized into different systems to calculate the GND densities. There are only 6 independent screw GND dislocations in *fcc* materials and hence, the GND dislocation space is discretized into 30 GND systems corresponding to 6 screw dislocations and 2 sets of 12 edge dislocations. The Nye tensor Λ can then be evaluated by summing up the contributions from each GND system as:

$$\Lambda = \sum_{\zeta=1}^{30} \rho_{GND}^\zeta \mathbf{b}^\zeta \otimes \mathbf{t}^\zeta; \text{ or in a vectorial form} : \{\lambda\} = [\mathbf{A}]\{\rho_{GND}\}$$
$$(34)$$

Here $\mathbf{b}^\zeta$ and $\mathbf{t}^\zeta$ designate respectively the Burgers and tangent vectors of the ζ th GND system. $\{\lambda\}$, $\{\rho_{GND}\}$ and $[\mathbf{A}]$ are (9×1), (30×1) and (9×30) matrices with the forms:

$$\{\lambda\} = \{\Lambda_{11} \quad \Lambda_{12} \quad \Lambda_{13} \quad \Lambda_{21} \quad \Lambda_{22} \quad \Lambda_{23} \quad \Lambda_{31} \quad \Lambda_{32} \quad \Lambda_{33}\}^T$$
$$\{\rho_{GND}\} = \{\rho_{et}^{(1)} \cdots \rho_{et}^{(1)}, \rho_{en}^{(1)} \cdots \rho_{en}^{(1)}, \rho_s^{(1)} \rho_s^{(2)} \rho_s^{(3)} \rho_s^{(4)} \rho_s^{(6)} \rho_s^{(8)}\}^T$$
$$\text{and} \quad [\mathbf{A}] = \begin{bmatrix} b_1^{(1)}t_1^{(1)} & b_1^{(2)}t_1^{(2)} & \cdots & b_1^{(30)}t_1^{(30)} \\ b_1^{(1)}t_2^{(1)} & b_1^{(2)}t_2^{(2)} & \cdots & b_1^{(30)}t_2^{(30)} \\ \cdot & \cdot & \cdots & \cdot \\ \cdot & \cdot & & \cdot \\ b_3^{(1)}t_3^{(1)} & b_3^{(2)}t_3^{(2)} & \cdots & b_3^{(30)}t_3^{(30)} \end{bmatrix} \qquad (35)$$

Eq. (34) is an inconsistent system of 9 equations and 30 unknowns. A least squares solution that minimizes the error $\|\{\lambda\} = [\mathbf{A}]\{\rho_{GND}\}\|$ yield the following problem to be solved:

$$[\mathbf{A}]^T[\mathbf{A}]\{\rho_{GND}\} = [\mathbf{A}]^T\{\lambda\} \qquad (36)$$

4.2. 3D virtual polycrystalline microstructure simulation and mesh generation

Virtual polycrystalline microstructures are generated using methods and codes described in Groeber et al. (2008a,b) and Thomas et al. (2012), by matching morphological and crystallographic statistics obtained from EBSD data of microstructural sections. The virtual 3D models have distributions of orientation, misorientation, microtexture, grain size and number of neighbors that are statistically equivalent to those observed experimentally in the OIM scans. The method estimates 3D statistics from extrapolation of 2D surface measurements and data on polycrystalline specimens. The reconstruction algorithm is based on stereology, a method of creating statistically equivalent 3D morphologies from 2D measurements. Grains are allowed to assume appropriate shapes when placed in the ensemble. The morphological orientations of virtual grains are assumed to be random and they are placed in the aggregate based on neighborhood constraints. The average number of neighbors is assumed to be approximately 14 grains, with some variation according to grain size. It has been seen that the number of neighbors of a grain is strongly correlated to its size. Once the voxelized morphological structure has been built, the grains and colonies with *fcc* lattice structure are assigned orientations based on a random sampling from the orientation distribution functions. Misorientation and micro-texturing statistics are matched by an iterative process, where orientations are allowed to switch between grains or be replaced by new random
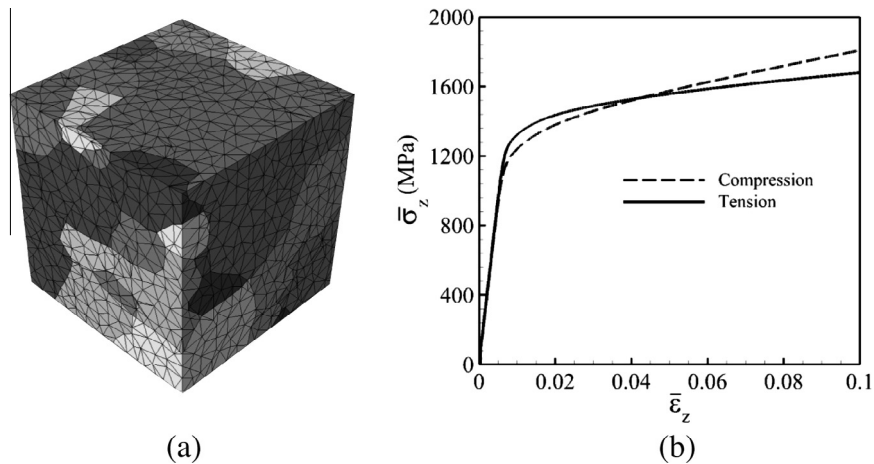
Fig. 12. Simulating polycrystalline microstructural behavior for Ni-based superalloys using the homogenized crystal plasticity model: (a) virtual polycrystalline microstructure showing the CPFEM mesh and (b) averaged true stress-logarithmic strain response from CPFEM simulations in tension and compression under an applied constant strain rate 0.0001 s^{-1}.

orientations until convergence is attained. Fig. 12(a) shows a statistically equivalent polycrystalline microstructural RVE of dimensions 15 μm × 15 μm × 15 μm containing 62 synthetically generated grains. The commercial mesh generator Simmetrix is used to generate 3D finite element mesh with 10,877 tetrahedral elements.

4.3. Results of polycrystalline microstructure simulation

Material parameters for the elastic-crystal plasticity constitutive model are the same as those calibrated in Sections 3.1 and 3.2. The sub-grain considered has a regular array of cubic precipitates with a 70% precipitate volume fraction and cubic γ' edge-length of 0.45 μm. Simulations are done for applied tension and compression strain-rate of 0.0001 s^{-1} in the z-direction at a temperature of 750 °C. A tensile constant strain-rate is applied to the top z-surface, while rigid body modes are suppressed by applying boundary conditions on the bottom z-surface as: $u_z = 0$ on all nodes $u_x = 0$ on nodes on the line $x = 7.5$ μm and $u_x = 0$ on nodes on the line $y = 7.5$ μm. $y = 7.5$ μm. The volume-averaged stress–strain responses for tension and compression are shown in Fig. 12(b). There is a significant difference between compression and tension responses resulting from the differential activation of APB shearing and micro-twinning. Each of these mechanisms is triggered based on load direction, crystal orientation and morphology of the microstructure. Both tension and compression simulations see a combination of APB shearing and micro-twinning. However for tension loading, the effect of micro-twinning is higher than for compression due to crystal orientation, which is evident from the lower plastic slope.

5. Summary and conclusions

This paper creates a hierarchical framework for realizing a homogenized grain-scale crystal plasticity model that can be used for modeling polycrystalline microstructures of Ni-based superalloys. Specifically, an activation energy-based crystal plasticity (AE-CP) FEM model is developed that incorporates characteristic parameters of the sub-grain scale $\gamma - \gamma'$ morphology. Hardening evolution laws are developed to reflect the effect of dislocation density distributions from the sub-grain RVE model, which represents deformation mechanisms in the temperature range 650 °C $\leqslant \theta \leqslant$ 800 °C. A significant advantage of this homogenized

AE-CP model is that its high efficiency enables it to be effectively incorporated in polycrystalline crystal plasticity FE simulations, while retaining the accuracy of detailed RVE models. It would be impossible to simulate polycrystalline microstructures with direct numerical simulation of the subgrain morphology otherwise. The homogenized model incorporates the effect of important characteristics of the sub-grain $\gamma - \gamma'$ morphology, viz. the volume fraction and shape of the γ' precipitates and the γ channel-width. Parametric representations of these sub-grain morphology variables are incorporated in evolution laws of the homogenized AE-CP model that include both thermal and athermal shear resistance. The simplified RVEs with uniformly distributed generalized ellipsoidal particles provide a demonstrative platform for modeling framework connecting three-scales, one with explicit representation and the others with their respective parametric forms. Three homogenized parameters, viz. the thermal shear resistance, the saturation shear resistance and the reference slip-rate $\dot{\gamma}_*$ are expressed as functions of the sub-grain morphology variables. Size dependence that is explicitly represented in the sub-grain dislocation density crystal plasticity model through the presence of geometrically necessary dislocations or GNDs, is reflected in the homogenized AE-CP model through the explicit dependence on the channel-width. The homogenized AE-CP model is found to accurately reproduce the stress–strain response of the detailed $\gamma - \gamma'$ RVE for a range of microstructural variations. It is also found to agree quite well with results of experimental studies on single crystal superalloys in the literature.

The other dominant mechanism at the grain-scale is micro-twinning, which is taken into account through a micro-twin nucleation and evolution model that is incorporated alongside the homogenized AE-CP model. Tension–compression asymmetry, observed in creep experiments, is very well represented by this model. In the final ascending scale in this paper, a polycrystalline microstructure of Ni-based superalloys is modeled using the homogenized CPFE model together with microtwinning. The grain-scale model is augmented through the accommodation of GNDs in the hardness formulations to compensate for lattice incompatibility. A statistically equivalent, virtual polycrystalline microstructural model of the superalloy CMSX is created for simulating polycrystalline behavior. This polycrystalline constitutive model implicitly retains the effect of microstructure morphology while reducing computational cost by several orders of magnitude without significant loss of accuracy. This is necessary for meaningful simulations that can be corroborated by experiments and can

be used to design morphology of the microstructure for improved performance.

Acknowledgement

This work has been partially supported by the US National Science Foundation, Civil and Mechanical Systems Division through Grant No. CMMI-0800587 (program manager: Dr. Clark Cooper), and by US Air Force Office of Scientific Research through Grant No. FA9550-13-1-0062 (program manager: Dr. David Stargel). This sponsorship is gratefully acknowledged. Computer use of the Hopkins High Performance Computing facilities is gratefully acknowledged.

References

Acharya, A., Beaudion, A.J., 2000. Grain-size effect in viscoplastic polycrystals at moderate strains. J. Mech. Phys. Solids 48, 2213–2230.

Arsenlis, A., Parks, D., 1999. Crystallographic aspects of geometrically-necessary and statistically-stored dislocation density. Acta Mater. 47, 1597–1611.

Arsenlis, A., Parks, D., 2002. Modeling the evolution of crystallographic dislocation density in crystal plasticity. J. Mech. Phys. Solids 50, 1979–2009.

Asaro, R.J., Needleman, A., 1985. Texture development and strain hardening in rate dependent polycrystals. Acta Mater. 33, 923–953.

Asaro, R.J., Rice, J.R., 1977. Strain localization in ductile single crystals. J. Mech. Phys. Solids 25, 309–338.

Busso, E., Meissonier, F., O'Dowd, N., 2000. Gradient-dependent deformation of two-phase single crystals. J. Mech. Phys. Solids 48, 2333–2361.

Chatterjee, D., Hazari, N., Das, N., Mitra, R., 2010. Microstructure and creep behavior of DMS4-type nickel based superalloy single crystals with orientations near <001> and <011>. Mater. Sci. Eng. A528, 604–613.

Choi, Y.S., Parthasarathy, T.A., Dimiduk, D.M., Uchic, M., 2005. Numerical study of the flow responses and the geometric constraint effects in Ni-base two-phase single crystals using strain gradient plasticity. Mater. Sci. Eng. A 397, 69–83.

Cormier, J., Milhet, X., Mendez, J., 2007. Non-isothermal creep at very high temperature of the nickel-based single crystal superalloy. Acta Mater. 55, 6250–6259.

Dimiduk, D.M., Uchic, M.D., Parathasarathy, T.A., 2005. Size-affected single-slip behavior of pure nickel microcrystals. Acta Mater. 53, 4065–4077.

Epishin, A., Link, T., Brückner, U., Portella, P.D., 2001. Kinetics of the topological inversion of the γ/γ'-microstructure during creep of a nickel-based superalloy. Acta Mater. 49, 4017–4023.

Fedelich, B., 2002. A microstructural model for the monotonic and the cyclic mechanical behavior of single crystals of superalloys at high temperatures. Int. J. Plast. 18, 1–49.

Fleury, G., Schubert, F., Nickel, H., 1996. Modeling of the thermo-mechanical behavior of the single crystal superalloy CMSX-4. Comput. Mater. Sci. 7, 187–193.

Fromm, B.S., Chang, K., McDowell, D.L., Chen, L., Garmestani, H., 2012. Linking phase-field and finite-element modeling for process–structure–property relations of a Ni-base superalloy. Acta Mater. 60, 5984–5999.

Frost, H.J., Ashby, M.F., 1982. Deformation-Mechanism-Map, The Plasticity and Creep of Metals and Ceramics. Perg. Press, Oxford.

Ghosh, S., 2011. Micromechanical Analysis and Multi-Scale Modeling Using the Voronoi Cell Finite Element Method. CRC Press/Taylor & Francis, ISBN: 978-1-4200-9437-4.

Ghosh, S., Anahid, M., 2013. Homogenized constitutive and fatigue nucleation models from crystal plasticity FE simulations of Ti alloys, Part 1: Macroscopic anisotropic yield function. Part 1. Int. J. Plast. 47, 182–201.

Ghosh, S., Bai, J., Paquet, D., 2009. Homogenization-based continuum plasticity-damage model for ductile failure of materials containing heterogeneities. J. Mech. Phys. Solids 57, 1017–1044.

Groeber, M.J., Ghosh, S., Uchic, M.D., Dimiduk, D.M., 2008a. A framework for automated analysis and simulation of 3D polycrystalline microstructures. Part 1: Statistical characterization. Acta Mater. 56, 1257–1273.

Groeber, M.J., Ghosh, S., Uchic, M.D., Dimiduk, D.M., 2008b. A framework for automated analysis and simulation of 3D polycrystalline microstructures. Part 2: Synthetic structure generation. Acta Mater. 56, 1274–1287.

Haghighat, S.M.H., Eggeler, G., Raabe, D., 2013. Effect of climb on dislocation mechanisms and creep rates in γ'-strengthened Ni base superalloy single crystals: a discrete dislocation dynamics study. Acta Mater. 61, 3709–3723.

Hill, R., 1984. On macroscopic effects of heterogeneity in elastoplastic media at finite strain. Math. Proc. Cambridge Philos. Soc. 95, 481–494.

Hong, H.U., Kim, I.S., Choi, B.G., Kim, M.Y., Jo, C.Y., 2009. The effect of grain boundary serration on creep resistance in a wrought nickel-based superalloy. Mat. Sci. Eng. A 517 (1–2), 125–131.

Ignat, M., Buffiere, J.Y., Chaix, J.M., 1993. Microstructures induced by a stress gradient in a nickel-based superalloy. Acta Mater. 41, 855–862.

Jain, J., Ghosh, S., 2008. Homogenization based 3d continuum damage mechanics model for composites undergoing microstructural debonding. ASME J. Appl. Mech. 75 (3), 031011-1–031011-15.

Kakehi, K., 1999. Tension/compression asymmetry in creep behavior of a Ni-based superalloy. Scr. Mater. 41 (5), 461–465.

Kalidindi, S.R., 1998. Incorporation of deformation twinning in crystal plasticity models. J. Mech. Phys. Solids 46, 267–290.

Karthikeyan, S., Unocic, R.R., Sarosi, P.M., Viswanathan, G.B., Whitis, D.D., Mills, M.J., 2006. Modeling microtwinning during creep in Ni-based superalloys. Scr. Mater. 54, 1157–1162.

Kayser, F.X., Stassis, C., 1981. The elastic constants of Ni3Al at 0 and 23.5 & #xB0;C. Phys. Status Solidi 64, 335–342.

Keshavarz, S., Ghosh, S., 2013. Multi-scale crystal plasticity fem approach to modeling nickel-based superalloys. Acta Mater. 61, 6549–6561.

Knowles, D.M., Gunturi, S., 2002. The role of <112>{111} slip in the asymmetric nature of creep of single crystal superalloy CMSX-4. Mater. Sci. Eng. A328, 223–237.

Kocks, U.F., Argon, A.S., Ashby, M.F., 1975. Thermodynamics and kinetics of slip. Progress in materials science. Prog. Mater. Sci. 19, 141–145.

Kovarik, L., Unocic, R., Li, J., Sarosi, P., Shen, C., Wang, Y., Mills, M., 2009. Microtwinning and other shearing mechanisms at intermediate temperatures in Ni-based superalloys. Prog. Mat. Sci. 54, 839–873.

Ma, A., Roters, F., 2004. A constitutive model for fcc single crystals based on dislocation densities and its application to uniaxial compression of aluminum single crystals. Acta Mater. 52, 3603–3612.

Ma, A., Roters, F., Raabe, D., 2006. A dislocation density based constitutive model for crystal plasticity FEM including geometrically necessary dislocations. Acta Mater. 54, 2169–2179.

Ma, A., Dye, D., Reed, R.C., 2008. A model for the creep deformation behavior of single-crystal superalloy CMSX-4. Acta Mater. 56, 1657–1670.

McLean, M., Cahn, R.W., 1996. Nickel-base Superalloys: Current Status and Potential, High Temperature Structural Materials. Chapman and Hall, London.

Nemat-Nasser, S., 1999. Averaging theorems in finite deformation plasticity. Mech. Mater. 31, 493–523.

Nouailhas, D., Cailletaud, G., 1996. Multiaxial behaviour of Ni-base single crystals. Scr. Mater. 34 (4), 565–571.

Nye, J.F., 1953. Some geometrical relations in dislocated crystals. Acta Metal. 1, 153–162.

Ohashi, T., Hidaka, K., Saito, M., 1997. Quantitative study of the plastic slip deformation and formation of internal stresses in Ni-base superalloys. Mater. Sci. Eng. A238, 42–49.

Pollock, T.M., Argon, A., 1992. Creep resistance of CMSX-3 nickel-base superalloy single-crystals. Acta Metall. 40, 1–30.

Pollock, T.M., Sammy, T., 2006. Nickel-based superalloys for advanced turbine engines: chemistry, microstructure, and properties. J. Prop. Power 22 (2), 361–375.

Probst, H., Dlouhy, A., Eggeler, G., 1999. Interface dislocations in superalloy single crystals. Acta Mater. 47, 2497–2510.

Roters, F., Eisenlohr, P., Hantcherli, L., Tjahjantoa, D.D., Bieler, T.R., Raabe, D., 2010. Overview of constitutive laws, kinematics, homogenization and multiscale methods in crystal plasticity finite-element modeling: theory, experiments, applications. Acta Mater. 58, 1152–1211.

Shenoy, M, 2006. Constitutive Modeling and Life Prediction in Ni-Base Superalloys (Ph.D. thesis). Georgia Inst. Tech.

Shenoy, M., Zhang, J., McDowell, D.L., 2007. Estimating fatigue sensitivity to polycrystalline Ni-base superalloy microstructures using a computational approach. Fatigue Fract. Eng. Mater. Struct. 30 (10), 889–904.

Song, J.E., 2010. Hierarchical Multiscale Modeling of Ni-base Superalloys (M.S. thesis). Georgia Inst. Tech.

Sugui, T., Jun, X., Xiaoming, Z., Benjiang, Q., Jianwei, L., Lili, Y., Wuxiang, W., 2011. Microstructure and creep behavior of FGH95 nickel-base superalloy. Mat. Sci. Eng. A528, 2076–2084.

Thomas, J., Groeber, M.J., Ghosh, S., 2012. Image-based crystal plasticity FE analysis for microstructure dependent properties of Ti-6Al-4V alloys. Mater. Sci. Eng. A. 553, 164–175.

Torster, F., Baumeister, G., Albrecht, J., Lütjering, G., Helm, D., Daeubler, M.A., 1997. Influence of grain size and heat treatment on the microstructure and mechanical properties of the nickel-base superalloy U 720 LI. Mater. Sci. Eng. A234–236, 189–192.

Unocic, R.R., Zhou, N., Kovarik, L., Shen, C., Wang, Y., Mills, M.J., 2011. Dislocation decorrelation and relationship to deformation microtwins during creep of a γ' precipitate strengthened Ni-based superalloy. Acta Mater. 59, 7325–7339.

Van Sluytman, J.S., Pollock, T.M., 2012. Optimal precipitate shapes in nickel-base c–c0 alloys. Acta Mater. 60, 1771–1783.

Viswanathan, G.B., Sarosi, P.M., Whitis, D.H., Mills, M.J., 2005. Deformation mechanisms at intermediate creep temperatures in the Ni-base superalloy Reńe 88 DT. Mater. Sci. Eng. A400, 489–495.

Xie, C.L., Ghosh, S., Groeber, M., 2004. Modeling cyclic deformation of HSLA steels using crystal plasticity. J. Eng. Mater. Technol. 126, 339–352.

Zambaldi, C., Roters, F., Raabe, D., Glatzel, U., 2007. Modeling and experiments on the indentation deformation and recrystallization of a single-crystal nickel-base superalloy. Mat. Sci. Eng. A454–455, 433–440.